

A Data-Driven Method for Measuring Position Resolution in the DEAP-3600 Dark  
Matter Detector  
By  
Joseph James Willis

A thesis submitted in partial fulfillment of the requirements for the degree of

Master of Science

Department of Physics  
University of Alberta

© Joseph James Willis, 2019

## ABSTRACT

DEAP-3600 is a single-phase liquid Argon dark matter detector operated at SNO-LAB in Ontario, Canada, searching for Weakly Interacting Massive Particles (WIMPs). It is well-established that astronomical and cosmological observations suggest the existence of some form of unseen matter in the universe, with the WIMP as one of the primary candidates. DEAP-3600 has set the leading limit on the WIMP-nucleon spin-independent cross-section for Argon based experiments, at  $3.9 \times 10^{-45} \text{ cm}^2$  ( $1.5 \times 10^{-44} \text{ cm}^2$ ) for a  $100 \text{ GeV } c^{-2}$  ( $1 \text{ TeV } c^{-2}$ ) mass WIMP (90% C.L.). A key factor in mitigating one source of backgrounds is the removal of events caused by contaminants on the inner surface of the acrylic vessel, achieved through means of position reconstruction and a fiducial cut on the reconstructed spherical radius. Understanding the precision of the reconstruction is therefore vital to knowing its effectiveness and so the goal of this project was to develop a method of measuring the position resolution in data. Using a process of event splitting this goal was achieved, demonstrating resolutions between 30 and 45 mm at the fiduciary boundary and at the energy range considered for candidate WIMP events.

## PREFACE

The hardware design and construction of the DEAP-3600 detector was done by members of the DEAP collaboration prior to my joining the experiment. Simulations and analysis were performed using the Reactor Analysis Tool (RAT) framework which was developed by members of the collaboration.

The position reconstruction programs detailed in Chapter 3 are the work of DEAP collaborators. The position resolution measurement method described in Chapter 4 however is my own work, except for where denoted by citations or explicit mention. My work has benefited from discussions with colleagues at the University of Alberta. The tools for this analysis have been added into the RAT framework.

The dust discrimination in a Toy Monte Carlo described in Chapter 5 is also my own work.

When I reach for the edge of the Universe, I do so knowing that along some paths of cosmic discovery, there are times when – at least for now – one must be content to love the questions themselves.

*Neil deGrasse Tyson*

## **ACKNOWLEDGEMENTS**

I would like to first and foremost thank my supervisor, Aksel Hallin, for taking me on and guiding me in this project, I wouldn't be here doing this if it wasn't for him. A huge thank you to my office-mates Tom and Courtney for always being willing to help, even when it was a stupid question or I just had a typo in my code. I thank my loving wife Karen, who provided support and encouragement when I struggled to get out of bed, accompanied me on adventures and continues to bring a smile to my face every day. I'm extremely grateful to my parents, Jim and Jeanne, who raised me in a loving home, who nurtured my curiosity and supported my passions, and who blessed me with the opportunity to go to university. I also could not have done this without my friends, thank you for the board games, ravine adventures and midnight Slurpee runs.

## TABLE OF CONTENTS

<b>Preface</b> . . . . .	iii
<b>Acknowledgments</b> . . . . .	v
<b>List of Figures</b> . . . . .	ix
<b>Glossary</b> . . . . .	xii
<b>Chapter 1: Introduction</b> . . . . .	1
1.1 Background . . . . .	1
1.2 Understanding the Standard Model . . . . .	9
1.3 Beyond the Standard Model . . . . .	11
1.3.1 Axions . . . . .	11
1.3.2 WIMPs . . . . .	12
1.4 Detection Methods . . . . .	12
1.4.1 Indirect Detection . . . . .	13
1.4.2 Production . . . . .	14

1.4.3	Direct Detection . . . . .	14
1.5	Null Results . . . . .	15
<b>Chapter 2: The Detector . . . . .</b>		<b>19</b>
2.1	Design Details . . . . .	19
2.2	Pulse-shape Discrimination . . . . .	22
2.3	Photomultiplication . . . . .	23
2.3.1	Photoelectric Effect . . . . .	24
2.3.2	Secondary Emission . . . . .	25
2.3.3	Photomultiplier Tubes . . . . .	26
<b>Chapter 3: Position Reconstruction . . . . .</b>		<b>28</b>
3.1	Charge-based Fitter . . . . .	28
3.2	Time-based Fitter . . . . .	29
3.3	Position Resolution . . . . .	37
<b>Chapter 4: Measuring Position Resolution . . . . .</b>		<b>38</b>
4.1	SplitEvent . . . . .	38
4.1.1	Radial Resolution . . . . .	46
4.1.2	Evaluation . . . . .	55
4.1.3	TIMEFIT2 Resolution . . . . .	60

4.2	MultiMB and Bias . . . . .	62
4.2.1	Continued Monitoring . . . . .	64
	<b>Chapter 5: Dust Hypothesis . . . . .</b>	<b>66</b>
	<b>Chapter 6: Conclusion . . . . .</b>	<b>70</b>
	<b>References . . . . .</b>	<b>75</b>
	<b>Appendix A: Fantastic Codes and Where to Find Them . . . . .</b>	<b>77</b>

## LIST OF FIGURES

1.1	The Coma Cluster . . . . .	2
1.2	Galaxy Rotation Curves . . . . .	4
1.3	The Bullet Cluster . . . . .	7
1.4	Angular Power Spectrum of the Cosmic Microwave Background . . . . .	8
1.5	The Standard Model . . . . .	10
1.6	Dark Matter Feynman Diagrams . . . . .	13
1.7	WIMP Limits . . . . .	16
1.8	Xenophobic WIMP Limits . . . . .	18
2.1	DEAP-3600 Schematic . . . . .	21
2.2	Electron and Nuclear Recoil Time Profiles . . . . .	23
2.3	Fprompt PE 2D Histogram . . . . .	24
2.4	Photomultiplier Tube Diagram . . . . .	27
3.1	TimeFit2 $\theta_{uv}$ Diagram . . . . .	31
3.2	Maximum/Minimum Time of Flight . . . . .	32

3.3	TimeFit2 PDF . . . . .	33
3.4	TimeFit2 PDF After Convolution . . . . .	34
3.5	Charge and Time Based Reconstruction Consistency . . . . .	35
3.6	Consistency Cut . . . . .	36
4.1	Pseudo-event Waveform . . . . .	39
4.2	1D Radius Difference Histogram . . . . .	41
4.3	Radial Parameter Widths Binned by Average Radius . . . . .	43
4.4	Single Run Radial Parameter Widths . . . . .	44
4.5	Time Evolution of Radial Parameter . . . . .	45
4.6	Characteristic Width Definition Test . . . . .	48
4.7	Multiple Run Resolutions . . . . .	49
4.8	Characteristic Width Definition Test 2 . . . . .	50
4.9	Resolutions Using the 2nd Central Moment . . . . .	51
4.10	Resolution Difference Using the 2nd Central Moment . . . . .	51
4.11	Percent Difference of Resolution Using the 2nd Central Moment . . . . .	52
4.12	Resolutions Found by Integration . . . . .	53
4.13	Resolution Difference Using the Integral . . . . .	54
4.14	Percent Difference of Resolution Using the Integral . . . . .	55
4.15	Resolution in Simulation Compared to Data . . . . .	56

4.16	SplitEvent Resolution in MC Compared to Truth-based Resolution . .	57
4.17	Bias in Reconstructed X-coordinate . . . . .	57
4.18	Radial Resolution Predictions and Results . . . . .	58
4.19	Resolution-Energy Comparison . . . . .	59
4.20	Resolution-Energy Fit . . . . .	60
4.21	Time-based Reconstruction Resolution . . . . .	61
4.22	Time and Charge-based Resolution Comparison . . . . .	61
4.23	Energy Bias in the X-Coordinate . . . . .	63
4.24	Energy Bias in the Y-Coordinate . . . . .	63
4.25	Energy Bias in the Z-Coordinate . . . . .	64
4.26	MultiMB Resolution Comparison . . . . .	65
5.1	Toy Monte Carlo Dust Discriminant . . . . .	67
5.2	Full Monte Carlo Dust Discriminant . . . . .	68
5.3	Fshadow Dust Discriminant . . . . .	69

## GLOSSARY

**AV** acrylic vessel. 19, 29, 30, 66, 68

**BSM** beyond-the-standard-model. 11, 12

**CDM** Cold Dark Matter. 6

**CMBR** Cosmic Microwave Background Radiation. 7, 8

**CP** charge-parity. 11

**DAQ** data acquisition. 26, 29

**GR** General Relativity. 3, 5, 6

**HQE** high quantum efficiency. 19

**HWHM** half-width-at-half-max. 47

**LAr** liquid Argon. 19, 22, 28, 42

**LG** light guide. 19, 30

**LIGO** Laser Interferometer Gravitational-Wave Observatory. 11

**m.w.e.** metre water equivalent. 19

**MC** Monte Carlo. 29, 32, 35, 37, 50

**MOND** Modified Newtonian Dynamics. 5, 6

**PDF** probability distribution function. 30, 32–34

**PE** photoelectron. 22, 35, 39, 41, 42, 45, 58, 62, 64, 69

**PMT** photomultiplier tube. 19, 20, 22, 23, 26, 28–30, 32–35, 38, 39, 59, 62, 64, 66, 68, 69

**PSD** pulse-shape discrimination. 22–24, 28

**RAT** Reactor Analysis Tool. iii

**ROI** Region of Interest. 28, 35, 66, 70

**SE** SplitEvent. 38, 57, 65

**SM** Standard Model. 9, 12, 14

**SNO** Sudbury Neutrino Observatory. 37, 40

**SUSY** Supersymmetry. 12, 13

**TeVS** Tensor-Vector-Scalar gravity. 6

**TF2** TimeFit2. 29, 35

**TOF** time-of-flight. 29

**TPB** Tetraphenyl butadiene. 19, 30, 66

**TPC** time projection chamber. 14

**WIMP** Weakly Interacting Massive Particle. 11–16, 22, 28, 35, 66, 69

# CHAPTER 1

## INTRODUCTION

### 1.1 Background

The true power of theories in physics is that they provide us with a model, i.e. a framework, for how the universe works, which lets us explain the things we observe and make predictions of the things we might be able to observe in the future. Newton's Universal Law of Gravitation provided an elegant and simple explanation to everything from an apple falling to the ground, to the moon's motion around the Earth, or even the distant Gallilean moons around Jupiter. It gave us a new tool to use in our study of the heavens, allowing us to quite literally "weigh" the Earth and determine its mass. Remarkably it even enabled astronomers to predict the very existence of an 8th planet in the Solar System. Observations of Uranus' orbit deviated ever so slightly from what was predicted by Newton's laws, and it was shown that another large planet in the outer Solar System could explain this difference. In 1846 the planet Neptune was first observed by Johann Gotfried Galle, only  $1^\circ$  off where French astronomer Urbain Le Verrier predicted it would be based on his calculations [1].

Modern astronomy has a similar question at hand regarding differences in observations and predictions of orbital motion in the large scale universe. It was first observed in the early twentieth century by Swiss astronomer Fritz Zwicky that galaxies in the Coma cluster (Figure 1.1) were moving too quickly to be gravitationally bound by the matter that could be inferred to be within them from their luminosity [2]. He found that there must be 400 times as much mass as could be seen (though more recent measurements show a smaller factor) and so he guessed at the existence of "dunkle Materie", or dark matter. A few decades later, American astronomer Vera Rubin and her colleagues measured the rotation rates of stars in galaxies and noticed a very peculiar trend. Newtonian physics predicts that as one moves further away from the galactic core, where



Figure 1.1: A mosaic of some of the galaxies within the Coma Cluster, taken by the Hubble Space Telescope.

much of a galaxy’s mass resides, the force of gravity decreases and the orbital speeds similarly decrease in turn. This is seen in our own solar system for instance, where Mercury being the closest planet to the Sun moves at a quick clip of 47.4 km/s but the far more distant Neptune orbits at a comparatively sluggish 5.4 km/s. Instead of seeing this trend play out in galaxies however, Rubin et al. observed the rotation curves shown in Figure 1.2, which flattened out at high speeds, even at the outer reaches of galaxies [3]. If we derive the speed of an object in orbit  $v$  at a distance  $R$  (Equation 1.1), we see that for velocity to remain constant the mass contained within the orbit ( $M$ ) must be increasing linearly with radius, or equivalently that the density  $\rho$  is proportional to  $R^{-2}$ . This conflicts with observations of stellar density that show a relationship of  $\rho \propto R^{-3.5}$  [4].

$$v(R) = \sqrt{\frac{GM(R)}{R}} \quad (1.1)$$

Just as in the galactic cluster case of Zwicky, this suggests that there is some additional mass spread through galaxies that is not observable to us through standard methods.

However missing mass is not always the solution to gravitational oddities. Another peculiarity within our own solar system was the observed precession of Mercury’s orbit. Planetary orbits are not perfectly circular but instead trace out ellipses, with the Sun located at one of the focal points. As a result the distance between a planet and the Sun is not constant but instead varies from a point of closest approach, known as perihelion, out to a most distant point, known as aphelion. In the mid-19th century it was discovered that the perihelion of Mercury had an anomalous precession, at an excess rate of 43 arcseconds/century [5]. This is around  $0.01^\circ$  every 100 years, a remarkable feat of astronomical observation at the time. Various explanations were put forth, including one by Le Verrier that proposed the existence of another small planet, similar to the case with Uranus and Neptune. This hypothesized planet “Vulcan” was thought to orbit between the Sun and Mercury, and many searches were carried out, but none were successful in locating it. Ultimately this mysterious precession was left unexplained until 1915 when Albert Einstein published his Theory of General Relativity.

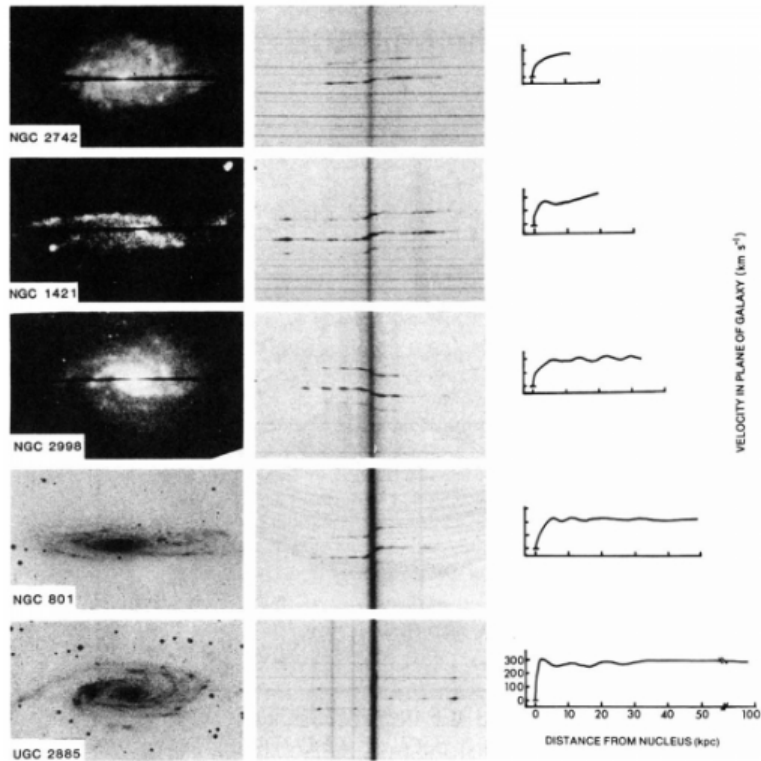


Figure 1.2: Five galaxies can be seen here, with the figures on the right showing the observed rotation rates as a function of distance from the centre of each galaxy [3]. In all of the cases the velocities remain flat rather than decreasing.

tivity (GR) [6]. His model explained gravity as the result of objects moving through spacetime that has been curved by the presence of mass or energy. Einstein applied his equations to the situation and discovered that the corrections coming from GR perfectly accounted for the extraneous drift. This was one of the first big successes of his theory, and many more came in the years following, all the way up to the 2015 direct detection of gravitational waves, one century after the publication of GR [7].

So we have seen now one case in which an unexplained discrepancy in the movement of heavenly bodies was solved by missing mass, and another case where it required the development of a new theory of gravity. It should come as no surprise then that not all astronomers and physicists are convinced that this missing gravity problem will be solved with missing mass. Israeli physicist Mordehai Milgrom proposed the first theory in a field that has since become known by the general label of modified gravity [8]. Proponents think that our understanding of gravity is still not yet complete, and that at galactic scales it behaves different to what we would predict using general relativity or Newtonian gravity. It is this difference that leads to the high orbital velocities of stars and galaxies, rather than unseen and unknown matter.

$$F_g = \frac{GMm}{\mu\left(\frac{a}{a_0}\right)R^2} \quad (1.2)$$

$$\mu\left(\frac{a}{a_0}\right) = \sqrt{\frac{1}{1 + \left(\frac{a_0}{a}\right)^2}} \quad (1.3)$$

Equation 1.2 shows a simple form of Modified Newtonian Dynamics (MOND) like that proposed by Milgrom, with  $\mu$  known as the standard interpolating function (Eq. 1.3). The constant  $a_0$  represents the transition point between the Newtonian and the MOND regimes. Milgrom fit this law to some galactic rotation curves and found  $a_0 \approx 1.2 \times 10^{-10} \text{ m s}^{-2}$ . When  $a \gg a_0$  it is plain to see that  $\mu \rightarrow 1$ , and given the incredibly small value of  $a_0$  this is the case in practically all circumstances on Earth. In the deep MOND regime where  $a \ll a_0$ , Eq. 1.2 simplifies to Eq. 1.4, which when acting as a centripetal force for an object undergoing circular motion ( $a = \frac{v^2}{R}$ ), yields

the result that the velocity is independent of  $R$  (Eq. 1.5).

$$F_g = \frac{GMm a_0}{R^2 a} \quad (1.4)$$

$$v^4 = GMa_0 \quad (1.5)$$

Various other models exist, including a relativistic generalization developed by Jacob Bekenstein in 2004 called Tensor-Vector-Scalar gravity (TeVeS). These theories have found moderate success at explaining galactic phenomenon but are not widely accepted within the mainstream scientific community, due to the continued successes of Einstein's theory of general relativity and a number of cosmological observations that are inconsistent with any modified gravity theories [9] [10].

The currently accepted model in cosmology is known as  $\Lambda$ CDM, referring to a cosmological constant ( $\Lambda$ ) for dark energy and Cold Dark Matter (CDM) to explain the gravitational effects. Dark energy is a topic outside the scope of this paper and is not related to dark matter, both terms use "dark" as a description of their mysterious nature to present day science. Put succinctly, the Universe appears to be speeding up in its expansion. This acceleration requires the presence of some sort of negative pressure inherent to the vacuum of space, which can be described in GR by a cosmological constant. This is an added term in the Einstein field equations that was originally included to try and create a static universe, but was later removed when it was discovered that the Universe was expanding. With the recent discovery of the accelerated expansion it is often put back into the equations to account for dark energy.

There are several examples of evidence that strongly favours the existence of actual dark matter particles over the explanation using modified gravity. First, in 2004 two papers were published on the Bullet Cluster: a galactic cluster merger over 3 billion lightyears away, which suggest it demonstrates a mass discrepancy that cannot be accounted for by MOND [11] [12]. Observed in X-rays, the collision showed a large amount of heated gas at the center of the merger, which had been stripped away as the clusters passed through each other. However using gravitational micro-lensing measurements in visible light, it was shown that much of the mass of the clusters was in

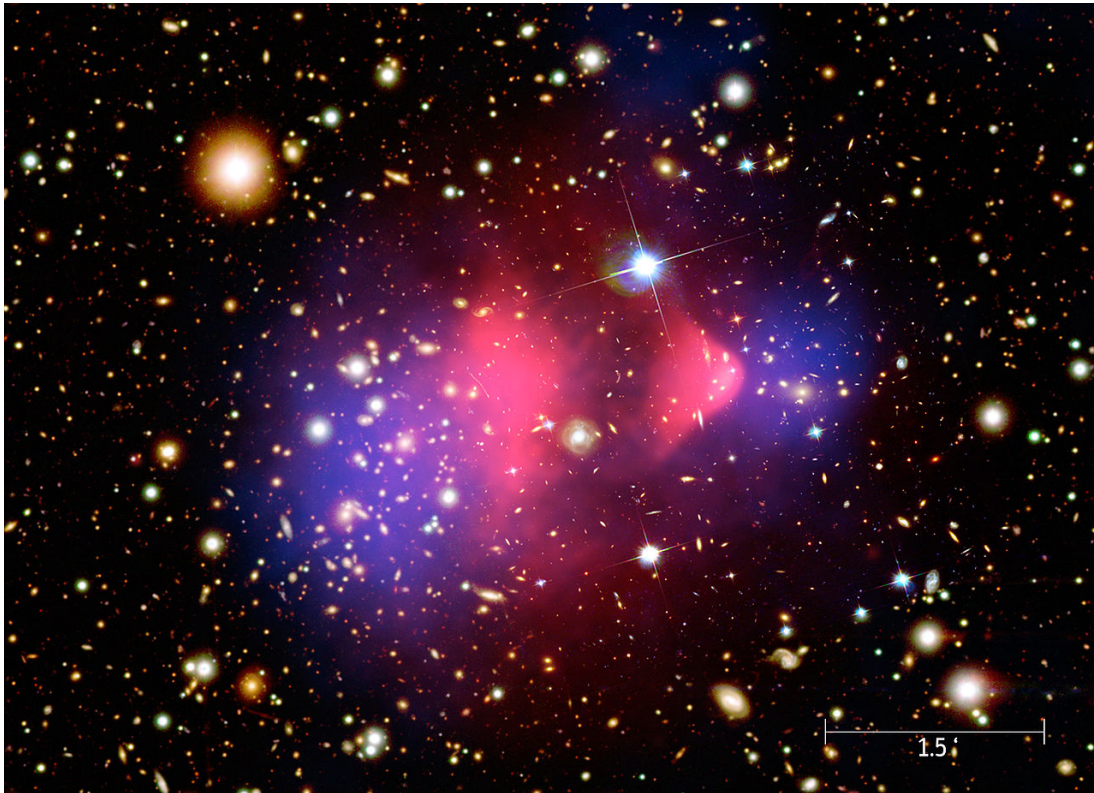


Figure 1.3: This image of the Bullet Cluster shows the X-ray emissions detected by the Chandra space telescope in pink and the mass distribution calculated using microlensing surveys in blue. By NASA/CXC/M. Weiss - Chandra X-Ray Observatory

two separate groups on either side, having passed through without interacting (except gravitationally), refer to Figure 1.3. Since the hot gas represents most of the baryonic matter within the clusters, modified gravity theories would suggest that is also where the strongest lensing would be observed, which was not the case.

The second example comes from measurements of the Cosmic Microwave Background Radiation (CMBR), relic light emitted only a few hundred thousand years after the Big Bang once the Universe had cooled enough to allow neutral atoms to form from the plasma, which had previously been an opaque fog. This radiation is observed over the whole sky, and is the most perfect black body spectrum ever measured in nature

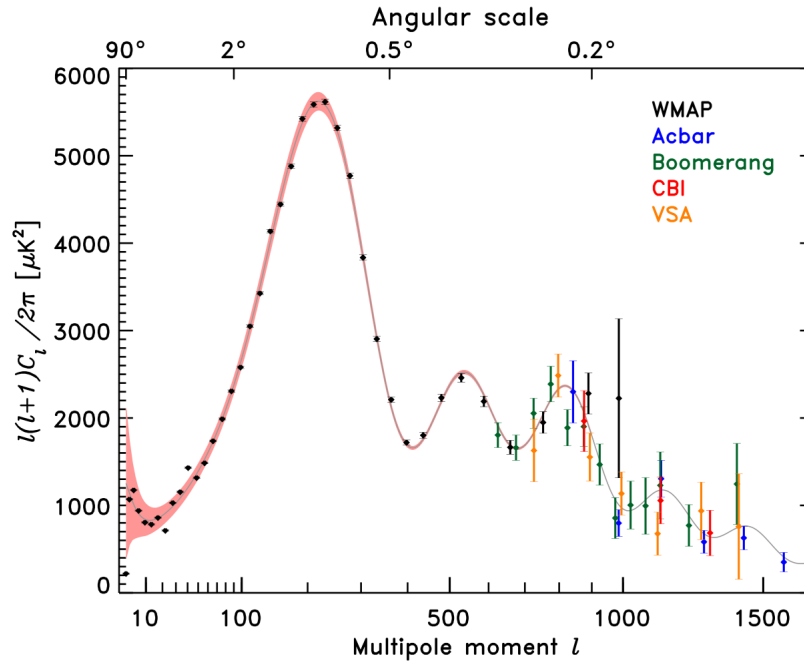


Figure 1.4: Data from five different experiments are shown for the CMBR's angular power spectrum. A theoretical model is shown as a black line, which is determined by the contents and properties of the universe. By NASA/WMAP Science Team - lambda.gsfc.nasa.gov

[13]. However, very small anisotropies exist on the order of  $10^{-5}$ , caused by over and under densities of the gas creating hotter and colder regions. It is by careful analysis of the angular power spectrum, essentially the size of the features within the CMBR, that a model for the components of the Universe can be tested, shown as the solid line in Figure 1.4. The latest results from the Planck collaboration find the Universe to consist of 69% dark energy, 26% dark matter and 5% baryonic matter [14].

The third example is the more recent discovery by astronomers of galaxies that appear to lack dark matter [15]. Somewhat counter-intuitively this missing dark matter is actually strong evidence for the existence of it as real particles. Modified theories of gravity should apply equally everywhere and so it should only be possible to not have the effect if dark matter is a real substance that could become decoupled from

baryonic matter. However that discovery has been called into question [16], so further observations by more groups will be required to definitively answer the question.

## 1.2 Understanding the Standard Model

Our understanding of particles and their interactions has come a long way since the discovery of the electron in 1897, and the combined theories are known as the Standard Model (SM). We know of three generations of matter; each containing two quarks, a charged lepton, and a neutrino. These are all fermions, particles with half-integer spin, meaning they obey the Pauli exclusion principle which prohibits two fermions from occupying the same quantum state in the same quantum system. This is what's responsible for the structure of electron orbits and ultimately the diverse chemical interactions that result. The interactions between fermions are due to four fundamental forces of nature: electromagnetism, gravity, strong nuclear and weak nuclear. As explained before, our best theory of gravity is Einstein's general relativity, and a particle-based explanation has not yet been verified. It is also far weaker than the other three forces at the level of individual particles. The remaining three forces are however explained by the exchange of bosons, particles with integer spin, meaning they are not subject to the Paul exclusion principle. The photon is the quanta of light and is responsible for mediating the electromagnetic interactions. Gluons are involved in the strong nuclear force which binds quarks together inside protons and neutrons. Lastly there is the weak nuclear force which has the charged  $W^\pm$  bosons and the neutral Z boson, and is responsible for radioactive beta decay and neutrino interactions. Finally there is the Higgs boson, the excitation of the Higgs field that is responsible for giving particles (although not neutrinos) their mass. All of these particles, including their properties such as mass or charge, can be seen in Figure 1.5.

However none of these particles are capable of describing the effects of dark matter. Any dark matter particle must be stable, at least on timescales of the Universe, as we see its effects in the early Universe as well as in the present era. This rules out the second and third generations of quarks, the muon and tau, the Higgs boson, as well as the  $W^\pm$  and Z bosons. It also needs to have mass, which eliminates the

# Standard Model of Elementary Particles

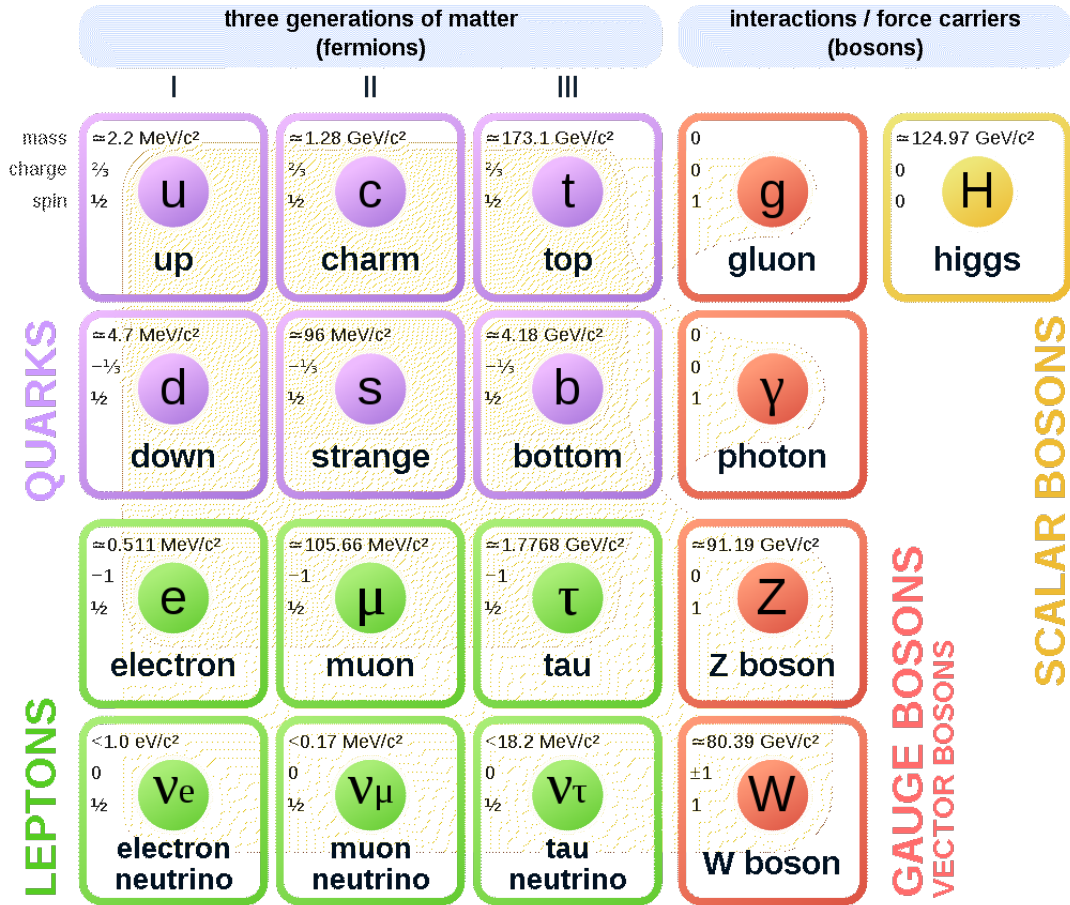


Figure 1.5: All the particles of the standard model, including their various properties such as mass, charge and spin. This image is used under the Creative Commons Attribution 3.0 Unported license, attribution to MissMJ.

photon and gluon from consideration. As stated it doesn't interact with light, neither scattering, absorbing nor emitting, and so must be electrically neutral, which rules out the electron and the up and down quarks. This leaves only the neutrinos, which at first present plausible candidates, but a final characteristic of the dark matter we observe is that it must be slow-moving in order to form the large-scale structures we find in the Universe. As the neutrinos have exceedingly small masses they tend to travel close to the speed of light when produced thermally, so while they do count as hot dark matter, they cannot account for any more than 6% of the DM mass in the Universe [17].

This forces us to look outside the Standard Model for an explanation to dark matter, in aptly named beyond-the-standard-model (BSM) theories. Two of the most prominent examples are the axion and the Weakly Interacting Massive Particle (WIMP).

### **1.3 Beyond the Standard Model**

#### 1.3.1 Axions

One of many happy accidents in physics, the axion came about first as a solution to what is known as the strong charge-parity (CP) problem, which stems from the strong nuclear force seeming to conserve CP but without clear reason why it should. It was discovered coincidentally that if axions exist and they have the right mass, they could be a potential candidate dark matter particle. They are predicted to be extremely low mass bosons, meaning that their average number density must be extremely large if they make up dark matter. Experimental searches for axions are still in the early phases. The most common methods involve using strong magnetic fields to convert axions into photons that could then be detected. However an arguably more fascinating proposal was given by Arvanitaki et al, who suggest that axions could gravitationally bind to black holes in a manner similar to electrons in atoms [18]. Then through a process known as superradiance, the black hole would create exponentially more axions. When axions transition between energy levels, or if they annihilate into gravitons, they would release gravitational waves akin to the emission of quantized photons in atoms. These waves could be detected by gravitational wave detectors like the Laser Interferometer

Gravitational-Wave Observatory (LIGO) and Virgo in the near future, and according to Arvanitaki would be “long-lasting, monochromatic, and can be distinguished from ordinary astrophysical sources.” Current searches of the conventional variety using magnetic fields have found no evidence of axions, with examples of some specific mass ranges considered being between  $0.31$  and  $8.3 \text{ neV c}^{-2}$  [19] and  $1.9$  to  $3.53 \mu\text{eV c}^{-2}$  [20].

### 1.3.2 WIMPs

These would be particles with masses typically considered in the range of  $\sim 1 \text{ GeV}$  (the mass of a proton) up to  $\sim 10^3 \text{ GeV}$ , and with cross sections up to the order of the weak nuclear force. As already explained, no such particle exists in the SM, but there are candidates in some BSM theories such as Supersymmetry (SUSY). Supersymmetry proposes the existence of a “superpartner” boson to every fermion in the SM, and a fermion to every boson. A key motivation for this theory is that it offers a solution to the Higgs boson’s small mass ( $125 \text{ GeV}$ ), which should be closer to the scale of the Planck mass  $\sim 10^{19} \text{ GeV}$  due to quantum corrections. The opposite signs of fermion and boson quantum corrections means that many will cancel in a supersymmetric theory [21]. The lightest supersymmetric particle is predicted to be stable and electrically neutral, as well as have similar masses and cross-sections ascribed to WIMPs.

This model for dark matter gained popularity among physicists due to the “WIMP miracle”, which showed that a  $100 \text{ GeV}$  particle that interacted through the electroweak force would “freeze out” in the early Universe at a density closely matching that of the measured dark matter. At present it is considered by many to be the most likely candidate for dark matter, although the continued absence of a positive detection is causing some to begin to rethink this notion. But the search is not done yet!

## **1.4 Detection Methods**

From this point on we will be assuming that dark matter is comprised of WIMPs. There are three basic ways that experimentalists can search for these particles, encapsulated

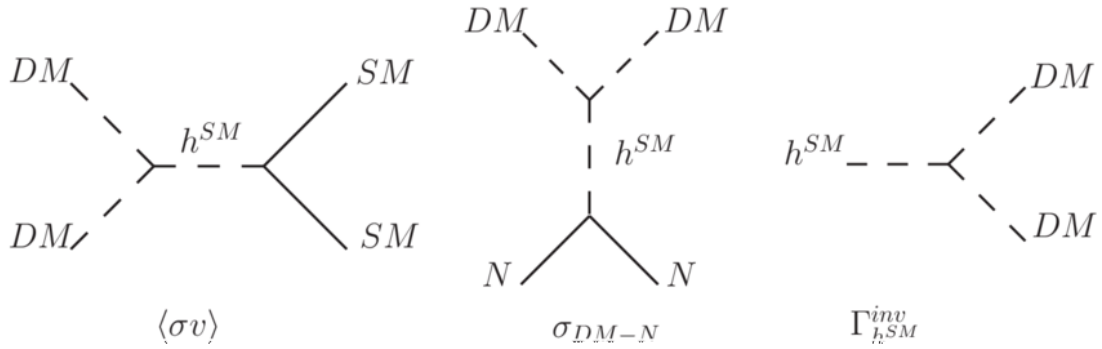


Figure 1.6: Three possible dark matter interactions mediated by the Higgs boson.

by the three Feynman diagrams in Figure 1.6, and explained in the following subsections. In all of the figures the interaction is mediated by a Higgs boson, however this is just one of many possible processes, with others being mediated via the Z boson or perhaps a particle from SUSY.

#### 1.4.1 Indirect Detection

If dark matter is self-annihilating, meaning it is its own anti-particle, then it is possible that the collision of two WIMPs could result in the creation of SM particles through an intermediary, such as the Higgs boson. This process is seen in the left-hand diagram of Fig 1.6, showing two dark matter particles annihilating into a Higgs that then decays to two standard matter particles. As such, indirect dark matter searches look for excess signals of particles such as positrons, gamma rays or neutrinos in regions where the expected dark matter density is higher, like in the central bulge of the Galaxy. This requires a careful consideration of other astronomical processes that could create the same products, so that the background level can be determined. Some of the strongest limits have been set by the South Pole-based neutrino detector IceCube, which probed self-interaction cross-sections as low as  $1.18 \times 10^{-23} \text{ cm}^3 \text{ s}^{-1}$  for a WIMP mass of  $100 \text{ GeV } c^{-2}$  [22].

### 1.4.2 Production

Seen in the far right diagram of Fig 1.6 is the production of two dark matter particles from a Higgs decay, which could be created by the interactions of standard model particles in high energy colliders such as the Large Hadron Collider. The generated WIMPs would certainly pass straight out of the detector without interacting, so the only trace they would leave is missing momentum. Results from the Tevatron experiment place limits just below  $10^{-38} \text{ cm}^2$  for spin-independent interactions, and just above  $10^{-40} \text{ cm}^2$  for spin-dependent, both at a WIMP mass of  $1 \text{ GeV } c^{-2}$  [23]. Spin-dependent interactions cannot be propagated by the Higgs due to its spin-0 nature. Instead they must be mediated by one of the weak bosons, for example.

### 1.4.3 Direct Detection

Last, and most important for this paper, is the direct interaction between dark matter and SM particles, seen in the centre diagram of Fig 1.6. There are a number of different ways that the energy deposited during scattering can be detected. Threshold detectors like PICO use a superheated liquid in a pressurized vessel. A nucleus recoiling off a dark matter particle can create a nucleation point around which a bubble can then form. Digital cameras outputting to an image processing program detect the bubbles and trigger the repressurization of the chamber. Piezoelectric acoustic sensors measure the waveform created by the collapsing bubbles, allowing for very strong discrimination between alphas and neutrons/WIMPs [24]. Because of the large energy deposition density required to cause nucleation, this detector is insensitive to electromagnetic backgrounds like gammas or betas. Another style of detector is the time projection chamber (TPC), which uses a series of uniform electric fields to accelerate ionization electrons produced by particle interactions in the target medium. Experiments such as XENON and LUX use cryogenic liquid Xenon in their detector which produces scintillation light when a particle deposits energy into it. This light creates the first signal, S1, picked up by arrays of photodetectors at the top and bottom of the chamber. Ionization electrons produced by the initial interaction are accelerated by the electric field towards the top of the detector where they enter the gas phase and transi-

tion into extremely strong electric extraction fields that cause rapid acceleration and the production of a second burst of scintillation light, the S2 signal. The timing difference between S1 and S2 allows for very accurate determination of the z position of the original event, and because the S2 signal happens very close to the upper photo-detection array it creates a clustering of charge that allows for accurate x-y reconstruction. The electrons scatter as they travel through the liquid, but the horizontal diffusion is typically on the order of millimetres over  $O(1 \text{ m})$  travel distances [25], so this does not have a large effect on position reconstruction. Lastly, there are experiments such as DEAP-3600 that uses cryogenic liquid Argon as a scintillating medium for the detection of particles. As this detector is the focus of the paper it will be described in further detail in Chapter 2.

## 1.5 Null Results

To date there has been no clear evidence of dark matter detection<sup>1</sup>, but even in the absence of any positive signal we can still learn a lot. By detecting no signs of it under specific conditions, we can work out what it *cannot be*. Null results from experiments are generally shown as an “exclusion curve”, which signifies what parameters have been ruled out and also allows for easy comparison between experiments using different target materials. For direct detection experiments like DEAP, they tend to follow the same general shape that can be seen in Figure 1.7. This type of plot shows the parameter space of possible WIMP-nucleon cross-sections and possible WIMP masses ( $M_\chi$ ). The region above the curve of a given experiment is what they have ruled out at 90% confidence due to an absence of a WIMP signal. Equation 1.6 shows that as the WIMP mass decreases, particularly for masses less than the target nucleus  $M_A$ , the mean energy that is deposited ( $\langle E_R \rangle$ ) from a scatter also decreases, making it more difficult to detect and reducing the detector’s sensitivity at lower masses[29]. Conversely, the energy-density of dark matter in the solar neighbourhood  $\rho_\chi$  is roughly

---

<sup>1</sup>DAMA-LIBRA has been seeing an annular modulation in count rate that they attribute to dark matter [26][27], but this is inconsistent with every other experiment and a plausible non-dark matter cause was given by Ferenc et al. [28]

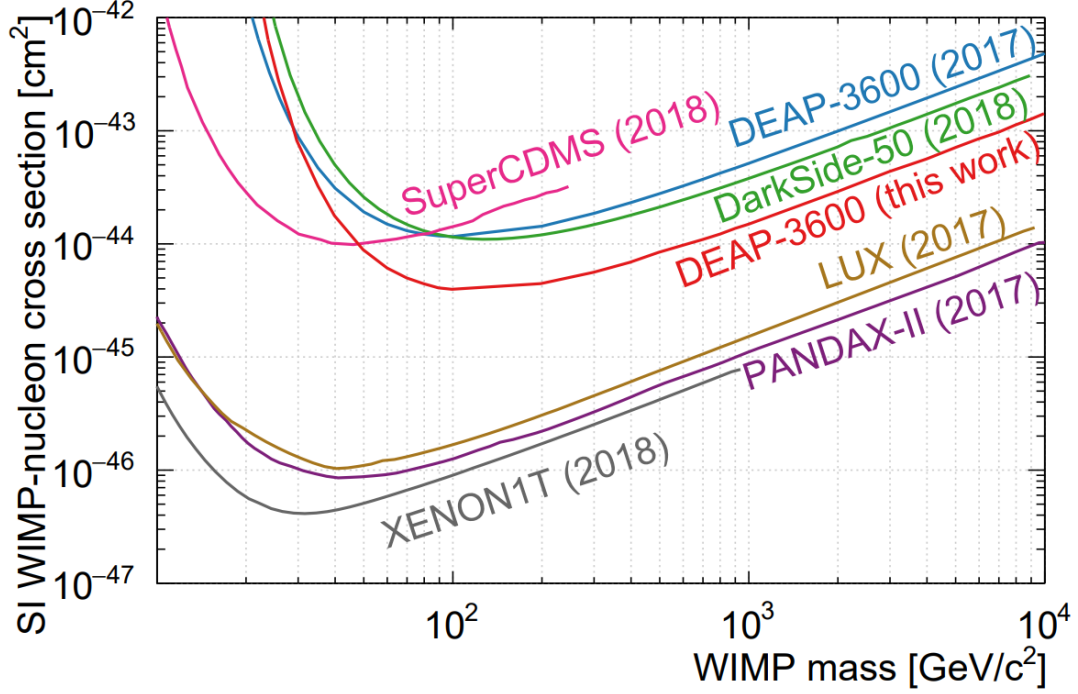


Figure 1.7: 90% confidence upper limit on the spin-independent WIMP-nucleon cross sections from a collection of direct detection experiments. The most recent result from DEAP-3600 as of this paper is shown as the solid red line [31].

$0.3 \text{ GeV } c^{-2} \text{ cm}^{-3}$ , and the resulting number density of WIMPs  $n_0$  is inversely proportional to the mass [29, 30]. This translates to a reduction in flux through the detector as the considered WIMP mass increases, which again limits what cross-sections you can rule out.

$$\langle E_R \rangle = r E_0 \propto \frac{v_0^2}{(1 + M_A/M_\chi)^2} \quad (1.6)$$

$$r = \frac{4M_\chi M_A}{(M_\chi + M_A)^2} \quad (1.7)$$

The Xenon based experiments XENON1T, PANDAX-II and LUX all lead the pack

for WIMP exclusion limits, beating out the Argon based experiments by roughly an order of magnitude at higher masses. This is due in part to the difference in atomic weight between the two elements, which gives Xenon an immediate advantage in sensitivity of roughly an order of magnitude. Figure 1.7 also shows the WIMP-nucleon cross-section under the assumption that the WIMP couples equally to protons and neutrons, however this is not the only possible case. In fact, if the coupling constants have opposite signs, it's possible to get a destructive interference between the proton and neutron contributions. Yaguna shows that for the right values of the neutron-to-proton coupling ratio the resulting suppression in Xenon is strong enough to actually make the DEAP-3600 results the most sensitive for WIMP masses above  $100 \text{ GeV } c^{-2}$ , see Figure 1.8 [32]. While this is a very particular case, it demonstrates that experiments of multiple target materials will be necessary in order to study the properties of WIMPs if they are detected.

Pushing to greater sensitivities, i.e. smaller cross-sections, requires low backgrounds, large masses and long exposure times. Those last two are in some ways interchangeable, as exposure is measured in kg days, but both are ultimately limited by the rate of backgrounds. Chapter 2 details the design of the DEAP-3600 detector and some of the many ways backgrounds are mitigated.

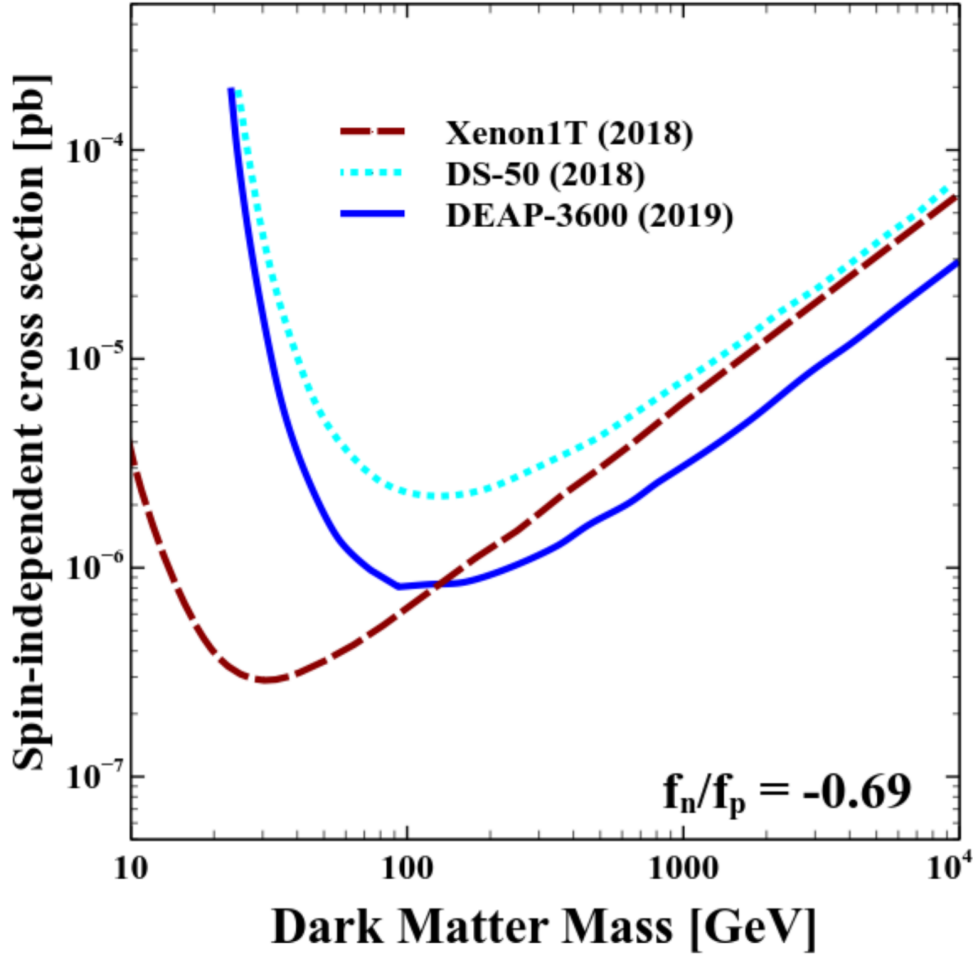


Figure 1.8: In the case of a neutron-to-proton coupling ratio of  $-0.69$ , the current exclusion curves from the XENON-1T, DS-50 and DEAP-3600 experiments are as shown. The destructive interference reduces the sensitivity in Xenon by a factor of almost four orders of magnitude but only around two orders in Argon [32].

## CHAPTER 2

### THE DETECTOR

#### 2.1 Design Details

Standing for ‘Dark matter Experiment using Argon Pulse-shape discrimination’, DEAP-3600 is a single phase liquid Argon detector stationed at Cube Hall in SNOLAB. This world-leading research facility is situated  $\sim 2$  km underground, or  $\sim 6000$  metre water equivalent (m.w.e.), at the Vale Creighton mine near Sudbury, Ontario, Canada. The heavy rock overburden provides critical shielding from cosmic rays, a necessity to achieve the low background rates needed for sensitive dark matter searches.

A cut-away schematic of the detector can be seen in Figure 2.1. The centre-piece of DEAP is the 1.7 m diameter acrylic vessel (AV), which holds the  $\sim 3300$  kg of liquid Argon (LAr). Extending upwards from the top of the vessel is the neck, which has a stainless steel cooling coil filled with liquid Nitrogen ( $\text{LN}_2$ ) that condenses the gaseous Argon as it flows past. Flow guides at the base of the neck direct the condensed LAr. Bonded to the outer surface of the AV are 255 acrylic light guides (LGs), each 45 cm long and optically coupled at the other end to a Hamamatsu R5912 high quantum efficiency (HQE) low radioactivity photomultiplier tube (PMT). The space between the LGs is filled with layers of high density polyethylene and Styrofoam filler blocks, as illustrated by the alternating blue and white lines in Fig 2.1. These filler blocks as well as the light guides provide shielding to the Argon from neutrons generated by the PMT glass, and also act as thermal insulation for the PMTs from the cryogenic LAr. This allows for the PMTs to run “warm”, at temperatures between 240 and 290 kelvin. The inner surface of the AV was shaved via a robotic tool to remove potential contaminants that could have adhered to the acrylic. It was then coated in a thin 0.3 mm layer of the wavelength shifter Tetraphenyl butadiene (TPB), which can absorb the UV scintillation light produced by interactions in the Argon, and re-emit photons in the visible range where the PMTs are more sensitive. The detector is then encased in a

stainless steel shell and submerged in a water tank, which provides additional shielding from gammas and neutrons produced in the surrounding rocks. On the outer surface of the steel shell are 48 outward-facing Hamamatsu R1408 PMTs, which operate as a muon veto that detects the Cherenkov radiation of cosmogenic muons passing through the water.

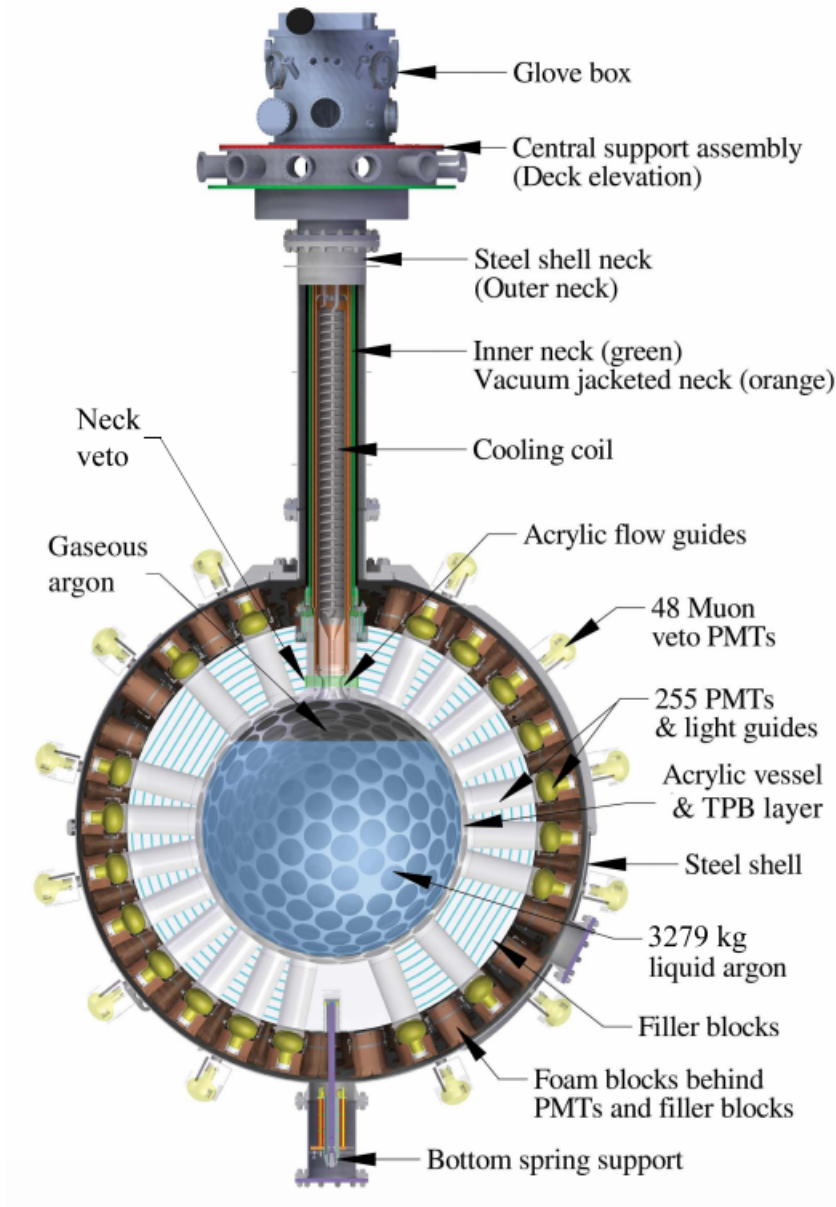


Figure 2.1: A cross-sectional view of the detector with labels of the key components.

## 2.2 Pulse-shape Discrimination

As its name suggests, a key aspect of the experiment relies on what is referred to as pulse-shape discrimination (PSD). When energy is deposited into the liquid Argon, through both electron scattering and nuclear recoils, excited Argon dimers (also sometimes called excimers) are created, which will de-excite non-radiatively until reaching a low energy singlet or triplet state. The decay from this final state releases 128 nm UV light, which does not have enough energy to create new dimers and thus passes uninhibited through the Argon. The singlet state has a short lifetime of  $\sim 6$  ns, while because the triplet state needs to go through a “forbidden” decay it is suppressed and has a much longer lifetime of  $\sim 1300$  ns. Ultimately the key to PSD is that the ratio of singlet to triplet states produced differs between nuclear recoils and electron scattering. When alphas, neutrons or WIMPs interact in the detector they scatter off the nucleus causing it to recoil. Due to the greater density of energy deposition, this recoil will generate a greater proportion of singlet states, which decay promptly [33]. Interactions from gammas and betas will interact with the Argon’s electrons and create more triplet states with their long decay times. The result is that the time profile of these two categories of events differ significantly and they can be discriminated through the use of a PMT parameter called  $F_{prompt}$ , see Equation 2.1 and Figure 2.2.

$$[h]F_{prompt} = \frac{\sum_{t=-28ns}^{t=60ns} PE(t)}{\sum_{t=-28ns}^{t=10\mu s} PE(t)} \quad (2.1)$$

This variable is calculated as the fraction of photoelectrons (PEs) detected in an early prompt period, for example the first 60 ns, relative to the total PE count of the event. Nuclear recoils with their greater singlet proportions will have a larger fraction of early light and tend to have  $\sim 0.7$   $F_{prompt}$  values, whereas electron recoils have more late light, which reduces the fraction to  $\sim 0.3$   $F_{prompt}$ . Figure 2.3 shows these two distributions over a range of PE counts.

Prior to DEAP-3600, the collaboration built and operated a proof-of-concept detector called DEAP-1, which housed 7 kg of LAr in an acrylic cylinder capped on either end by PMTs. With this experiment they were able to demonstrate a limit of

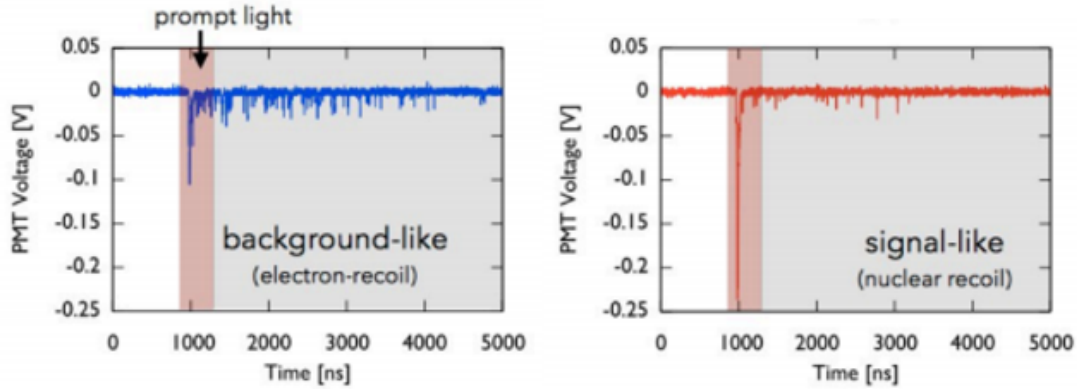


Figure 2.2: In the left hand plot the PMT voltage (where dips represent the detection of photoelectrons) is shown for an electron recoil event. The greater fraction of triplet states produced in the event causes more delayed light. The right plot shows a nuclear recoil event, where the excess singlet states cause most of the light to occur early.

$< 2.7 \times 10^{-8}$  (90% C.L.) contamination of electronic recoil events into the nuclear-recoil region of interest [33].

PSD is critical to the operation of DEAP-3600 due to the inherent EM background from the  $\beta$ -decay of Ar-39, a radioactive isotope produced by interactions with cosmic rays in the atmosphere. This creates a background rate of  $\sim 3.3$  kHz in the detector. So without strong discrimination of electron recoils, this would wash out any possible dark matter signal and greatly limit the sensitivity. Future large-scale Argon experiments may use underground Argon, which has vastly reduced Ar-39 concentrations due to being much older than the atmospheric variant used in DEAP.

### 2.3 Photomultiplication

As discussed earlier in the chapter, DEAP utilizes 255 photomultiplier tubes to detect the light produced by particles interacting in the liquid Argon. These light-sensing detectors have been around for almost a century, and utilize the photoelectric effect and secondary emission.

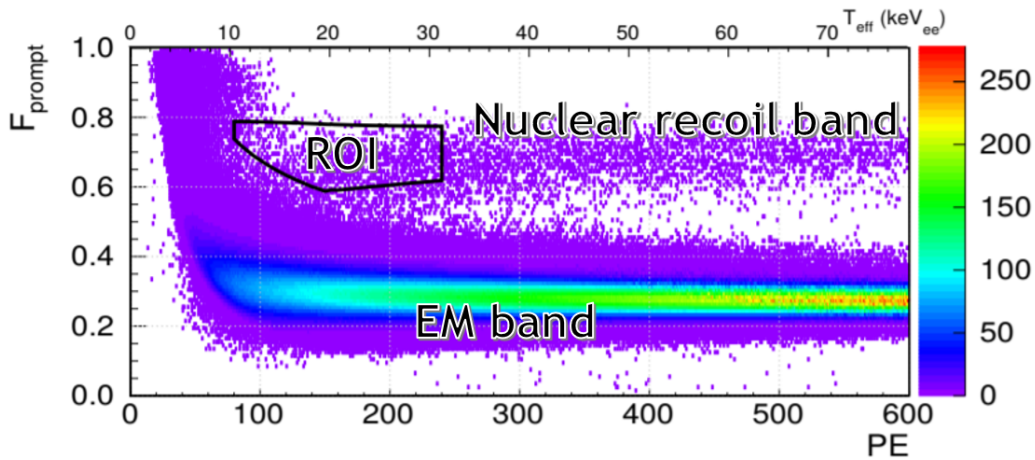


Figure 2.3: This 2D histogram shows events from a calibration run with a neutron source deployed. The vertical axis shows the PSD variable  $F_{\text{prompt}}$  and the horizontal axis displays the detected number of photoelectrons. The bright band at  $\sim 0.3 F_{\text{prompt}}$  comes from electron recoils, the vast majority of which are caused by  $\beta$ -decay of Ar-39. The band around  $0.7 F_{\text{prompt}}$  is from the nuclear recoils caused by the injected neutrons. The black box on the lefthand side shows the Region of Interest within which we search for candidate WIMP events.

### 2.3.1 Photoelectric Effect

In 1905 Albert Einstein published four revolutionary papers that helped birth multiple new fields of physics and are still of importance today, making it his ‘annus mirabilis’ or ‘year of miracles’ as it is now known. One of these papers was on the photoelectric effect, a peculiar phenomenon first observed in the late 19th century by Heinrich Hertz and later in 1902 by Phillip Lenard [34, 35]. When the surface of a metal was exposed to light it was observed to be emitting cathode rays (what we now know to be electrons); however the energy of the cathode rays seemed to depend only on the frequency of the light and not its intensity. This was not in accordance to the understanding of light as an electromagnetic wave, as Maxwell’s equations would predict that as the intensity of light upon the metal increased, the available energy would also increase and transfer more energy to the cathode rays. Einstein was able to explain this

phenomenon by creating ‘quanta’ of light energy called photons, and he used Planck’s law of black-body radiation to determine they would have an energy  $hf$ , where  $h$  is Planck’s constant and  $f$  is the frequency of light [36]. The electrons in the metal have some potential energy that must be overcome in order for them to be ejected from the surface which is known as the metal’s work function  $W$ . Therefore an electron’s kinetic energy could be described by the simple linear Equation 2.2. This explains why the energy of the emitted electrons depended on the frequency of light; increasing the intensity only increases the number of photons but if photons do not have enough energy to overcome the work function they can not kick electrons out. In 1916 famed experimentalist Robert A. Millikan published a paper demonstrating the linear relationship as predicted by Einstein, with an accurate measurement of Planck’s constant [37].

$$KE = hf - W \quad (2.2)$$

### 2.3.2 Secondary Emission

This effect is critical to photomultipliers as it causes an amplification of a signal, allowing detectors to measure down to the level of individual photons. In 1902 Austin and Starke were studying the scattering of electrons off metals and observed that the flux of outgoing electrons was occasionally greater than the incident flux [38]. When incoming electrons have sufficient energy they can free electrons in the material when scattering. These freed electrons are known as secondary electrons and are typically ejected with little kinetic energy. A single electron can create multiple secondary electrons, and so by applying an electric potential it is possible to accelerate these secondary electrons until they possess enough energy to scatter and free additional electrons. This produces an exponential increase in the number of flowing electrons, generally referred to as a Townsend avalanche in gas or an avalanche breakdown in insulators and semiconductors. It becomes possible to measure these pulses of electricity by amplifying the initial current multiple orders of magnitude.

### 2.3.3 Photomultiplier Tubes

The photomultiplier tube was invented in the early 1900s following the discovery of the photoelectric effect and secondary emission. It consists of a glass surface at the head of a long tube, as shown in Figure 2.4. This glass is coated with a thin metallic film and acts as a photocathode, releasing an electron when a photon of sufficient energy is absorbed. An electric potential is placed across the photocathode and the focusing electrode. This accelerates the photoelectron and guides it towards the first dynode. Secondary electrons are produced when the photoelectron strikes the dynode. A voltage step-up between the first and second dynode accelerates the secondary electrons so that when they reach the second dynode they can produce additional electrons. This is repeated several more times with additional dynodes and voltage steps, with the number of electrons increasing exponentially. At the final anode the current pulse exits and can be detected using data acquisition (DAQ) hardware and software. PMTs are capable of gains reaching  $10^6$ , producing one million electrons for each original photoelectron, meaning current pulses with charges on the order of a tenth of a picocoulomb. This process of amplification is extremely consistent making it possible to achieve timing resolutions on the order of 1 nanosecond or less for the PMTs in DEAP [39]. The digitizer that converts the analog signals into digital ones places the charge in bins 4 nanoseconds wide, but with fitting of the pulse charge-time distributions it is possible to get the resolution back down to sub-nanosecond timing.

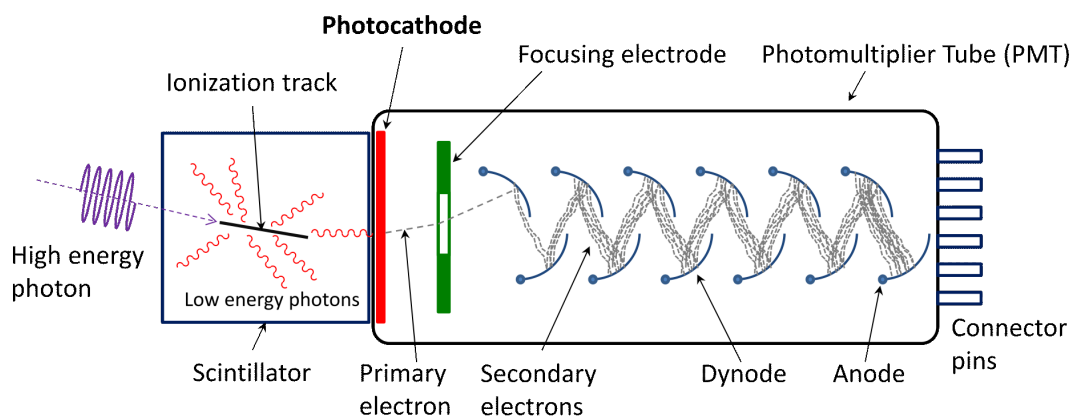


Figure 2.4: This 2D-cutaway diagram shows the key components of a photomultiplier tube, along with illustrations of the processes that occur when a photon is detected. This image is used under the Creative Commons Attribution-Share Alike 3.0 license, attribution to Qwerty123uiop.

## CHAPTER 3

### POSITION RECONSTRUCTION

It is important to know where in the detector volume an event happened, as this can often tell you something about the event. Arguably the most critical factor for DEAP after PSD is the proximity of events to the inner surface of the acrylic vessel. As discussed in Chapter 2 the inner acrylic vessel surface was shaved to remove any dust that may have settled on its surface during construction, but contaminants are still expected to exist within the acrylic. Alphas produced from the Radium decay chain can only travel tens of  $\mu\text{m}$  within the LAr and so any alphas that are generated at the surface will also deposit all of their energy there. Since alphas cause the nucleus to recoil when they scatter, they will have high  $F_{\text{prompt}}$  values, similar to those of WIMPs. Additionally, gamma radiation from the PMTs can interact in the acrylic and excite electrons that then produce Cherenkov radiation as they travel. These can also have high  $F_{\text{prompt}}$  and energies close to the WIMP Region of Interest (ROI), making them another class of surface background. By applying a cut to any events that reconstruct outside of a specified radius, known as a fiducial cut, it is possible to limit the leakage of these background events into the WIMP search region.

#### 3.1 Charge-based Fitter

The primary position reconstruction algorithm used by the DEAP collaboration is a charge-based likelihood fitter called MBLIKELIHOOD, named after its author Mikhail Batygov [40]. It works by finding the position that maximizes the likelihood that a given PMT would have seen the measured charge (occupancy) for an event occurring at that location and with the total reconstructed energy.

$$L = \prod_i f(q_i | \lambda_i) \tag{3.1}$$

It uses two parameters for determining the expected occupancy  $\lambda_i$ , which are i) the distance from the centre of the detector to the event (its radius) and ii) the cosine of the angle between the vectors pointing from the centre of the detector to the PMT and to the event. Equation 3.2 shows how the occupancy is calculated for the  $i^{th}$  PMT from an event with energy  $E$ , where  $k$  is the light yield factor and the  $R$  vectors are positions of the PMT and the event, respectively.

$$\lambda_i = kE\phi(\mathbf{R}_{\text{PMT}_i}, \mathbf{R}_*) \quad (3.2)$$

The function  $f(q|\lambda)$  in Equation 3.1 takes the shape of the Poisson function convoluted with the PMT response function, which is measured in the detector with the use of a light-injection system that sends carefully controlled pulses into the detector.

The fitter is trained using Monte Carlo (MC) simulations, which generate isotropic “photon bombs” at various points in the detector volume, using Chebyshev polynomials to fit each PMT’s equations and allow for smooth interpolation between the tested points. Additionally, the distribution of these test points is not uniform, but instead increases in density towards the AV surface as the functions change rapidly in this region. Doing this ensures that a higher resolution in position, approaching the Cramer-Rao limit, can be achieved for events near the surface. This vastly improves the effectiveness of the fiducial cut [40].

### 3.2 Time-based Fitter

Because of the size of the DEAP-3600 detector and the timing resolution made possible with its PMTs and DAQ system, event positions can also be reconstructed by utilizing the finite time-of-flight (TOF) of photons produced. This fitter goes by the name TIMEFIT2 (TF2), as it was the successor to a first algorithm that used a different methodology. Initial attempts at building this new fitter started with a similar procedure of using MC for training as was used in the charge-based fitter [41]. The detector volume was broken up into cells defined by a distance  $r$  from the face of a test light guide and an angle  $\sin \theta$  off the light guide axis. Photon bombs were generated

in each cell, with photons travelling at the UV group velocity until reaching the AV surface and being re-emitted by the TPB to then travel at the visible group velocity until finally reaching the LG. The total time of flight for each photon was calculated using Eq. 3.3 and then the solid angle of the LG from the point of re-emission is used to weight the histogram entry of the given time for the given cell.

$$\text{TOF}(\mathbf{p}, \mathbf{X}_0) = \frac{\|\mathbf{x}' - \mathbf{X}_0\|}{v_{\text{uv}}} + \frac{\|\mathbf{p} - \mathbf{x}'\|}{v_{\text{vis}}} \quad (3.3)$$

However this method was limited by statistics and led to discontinuities in the derivative that negatively affected the minimizer's ability to fit the position. To get around this an alternative approach was taken that instead numerically integrated the PMT response function. It still looked at cells at varying distances  $r$  and angles  $\sin \theta$ , but now instead of simulating photons generated at that point a calculation is done to find the minimum and maximum times of flight for a given angle dubbed  $\theta_{\text{uv}}$ . A diagram can be seen in Figure 3.1 that attempts to illustrate this, showing that  $\theta_{\text{uv}}$  is measured from the vector pointing from the centre of the detector to the considered event vertex. The possible directions a photon can travel at that  $\theta_{\text{uv}}$  create a cone when  $\phi_{\text{uv}}$  is varied from 0 to  $2\pi$ , which will then intersect the AV representing the possible TPB absorption and re-emission points. The x-axis ( $\phi_{\text{uv}} = 0$ ) is chosen to point in the direction of the PMT from the vertex, and  $\phi_{\text{uv}} = \pi$  is therefore away from the PMT. The two acrylic vessel intersection points corresponding to  $\phi_{\text{uv}} = 0$  and  $\phi_{\text{uv}} = \pi$  then represent the minimum and maximum distances, and therefore time, visible light can travel. For a given vertex, as  $\cos \theta_{\text{uv}}$  is varied from -1 to 1, the corresponding minimum and maximum times of flight are shown in Figure 3.2 as the blue and red lines, respectively. The area between these two curves that is within some  $t_1$  and  $t_2$  (the horizontal lines) represents the probability that the PMT would see light at that time (measured since the original time of the event  $T_0$ ) for an event at that vertex. So a probability distribution function (PDF) can be generated by varying  $r$  and  $\sin \theta$  and integrating for every 0.25 ns time window from 0 ns up to 40 ns, seen in Figure 3.3. The x-axis in the plot is divided into 170 regions, each representing 10 mm in  $r$ , and which are further divided into 100 equal bins for  $\sin \theta$  between 0 and 1. This PDF is

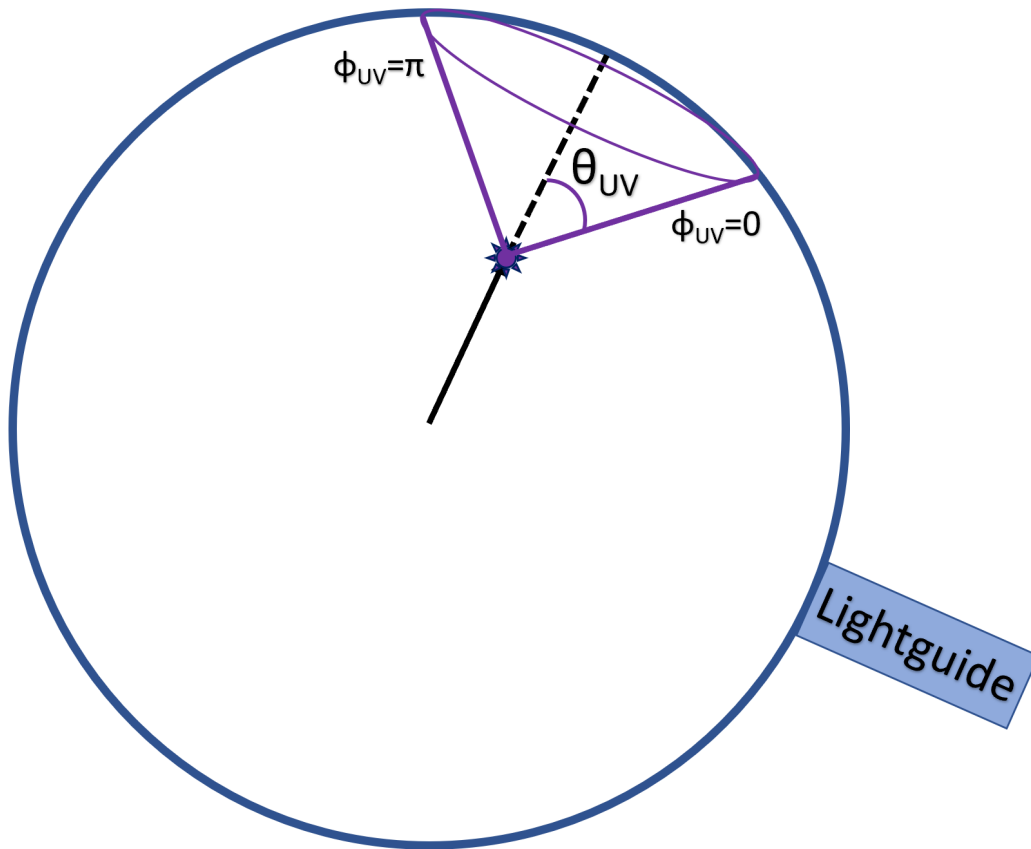


Figure 3.1: This drawing illustrates how for a given  $\theta_{uv}$ , the light from an event can travel in a cone with some value  $\phi_{uv} \in (0, 2\pi)$ , where  $\phi_{uv} = 0$  is chosen to point towards the lightguide being considered.

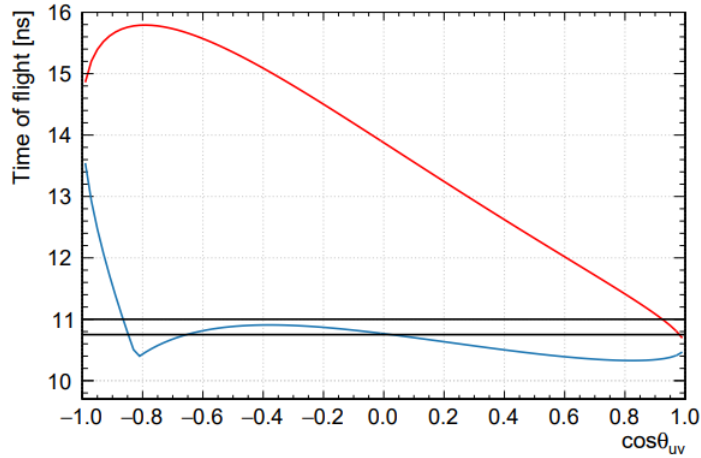


Figure 3.2: “An example showing the time of flight for a PMT at (0,0,850) and an event at (300,0,-250). No paths result in a time of flight below about 10 ns or above about 15.4 ns. The bottom blue line corresponds to the minimum time of flight at  $\phi_{uv} = 0$  and the top red line to the maximum with  $\phi_{uv} = \pi$ . The horizontal lines at 10.75 ns and 11 ns show a typical integration region. We integrate from the leftmost intersection with one of the curves to the rightmost in  $\cos \theta_{uv}$ . For each point in  $\cos \theta_{uv}$  we integrate in phi from the phi corresponding to the maximum of 10.75 ns and the bottom of blue curve, to the phi corresponding to the minimum of 11 ns and the top of red curve.” This figure and caption taken from [41]

then used during the fitting procedure, by moving the vertex and  $T_0$  around to minimize the total product of all the PMT probabilities. This can be written as the sum of the log-likelihoods:

$$\log(L) = \sum_i q_i \log(P(t_i; \mathbf{X}_0, t_0)) \quad (3.4)$$

Where  $P$  is the probability of an individual PMT seeing light at time  $t_i$  emitted from the test position  $\mathbf{X}_0$  at time  $t_0$ .

This method produced more smoothly varying PDFs, see Figures 3.3 and 3.4, than the MC version and allowed for more precise fits. However the resolution of this fitter was still consistently worse than that of the charge-based version, both in Monte Carlo and in data, as will be shown and discussed in more detail in a later chapter. Because of

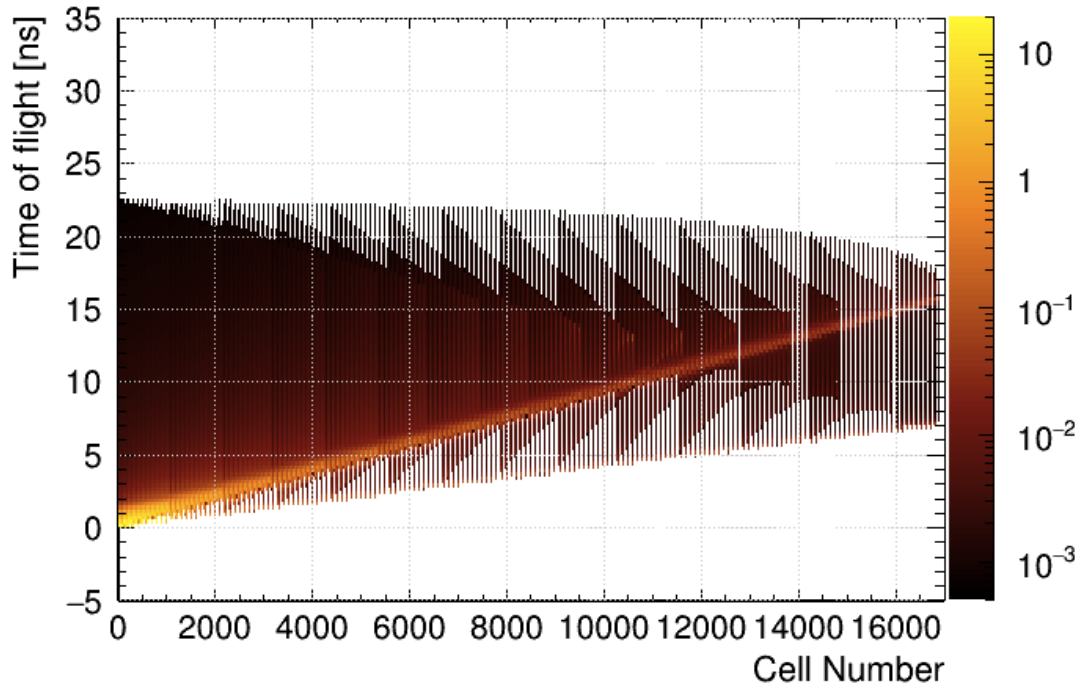


Figure 3.3: The PDF for the time-based fitter depends on the cell number (determined by the distance and angle from the PMT) and the time of the photon's arrival. The bright band going across the middle is from the UV light, while the narrower bright band that forms the bottom edge is the visible light, since its group velocity in Argon is greater [41]. The jaggedness visible is a Moire pattern due to the fine binning.

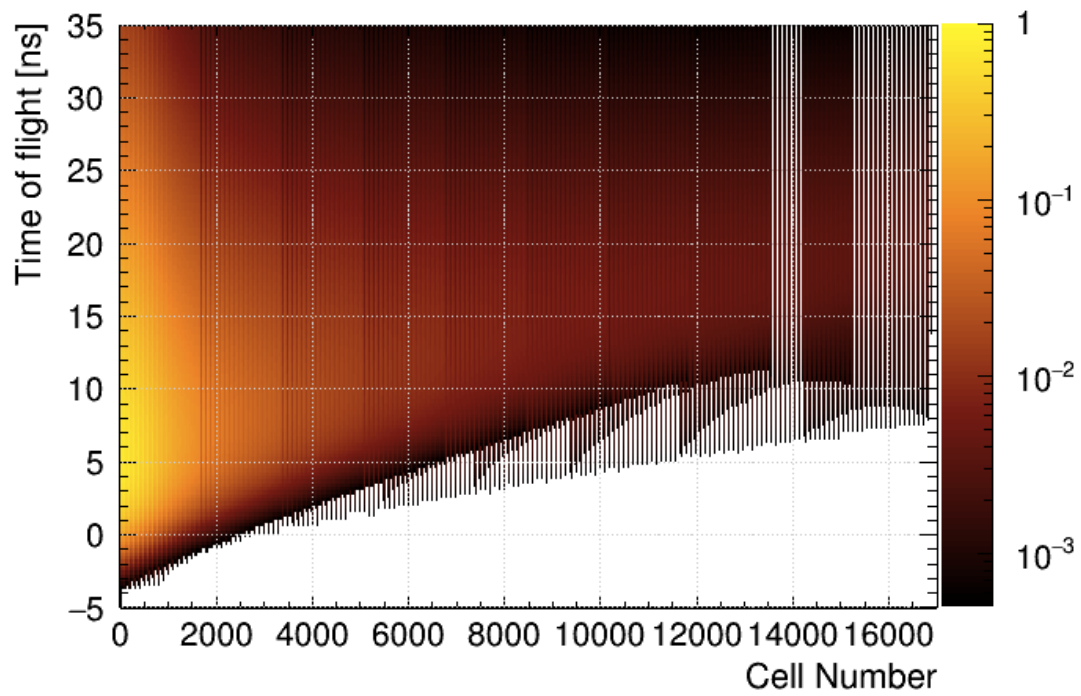


Figure 3.4: The same PDF from Figure 3.3 but now convoluted with the TPB timing and PMT response. This has the effect of smearing out the probabilities, as well as extending the possible time-of-flight [41].

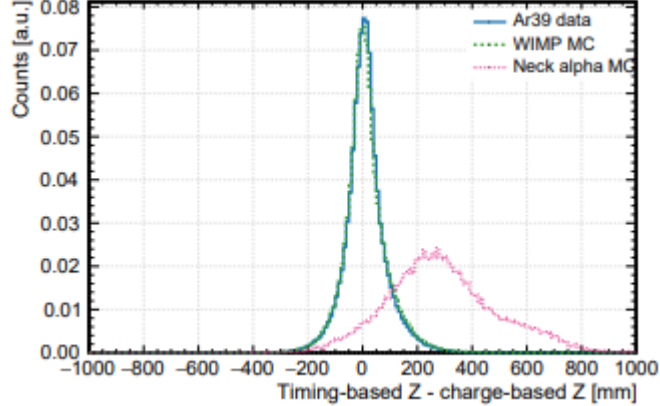


Figure 3.5: “Difference in reconstructed vertex position (left) and reconstructed Z (right) between TimeFit2 and MBLikelihood, shown for Ar39 data, WIMP MC (Ar40 nuclear recoils), and neck alpha MC. The events are selected as that the number of photoelectrons used in TimeFit2 is in range of 50 to 150 PE, which is approximately equivalent to ROI energy for nuclear recoils.” [41]

this the charge-based fitter remains the primary position reconstruction algorithm employed for performing the fiducial cut; however studies in MC showed that TF2 could be useful in discriminating alpha events in the neck region of the detector [41]. Events occurring in this part of the detector have been a consistently notorious background owing to the flow guides that shadow the light produced, causing most of the light to end up near the bottom of the detector. This distribution of hit PMTs tends to confuse the charge-based fitter, which places the vertex nearer to the bottom or at the centre of the detector. The time-based fitter however is not as challenged by this situation, and tends to put the vertex closer to the top of the acrylic vessel. While still not usually an accurate marker of the true position, this disagreement between the vertical positions of the two fitters was found to be a good discriminant for identifying these neck events, see Figure 3.5. A large fraction (90%) of these background events can be removed by cutting on any events that had a difference in fitted z-position between the two reconstructions greater than a value dependent on the prompt energy. Figure 3.6 shows the box used for this cut, with any event landing outside the line being removed.

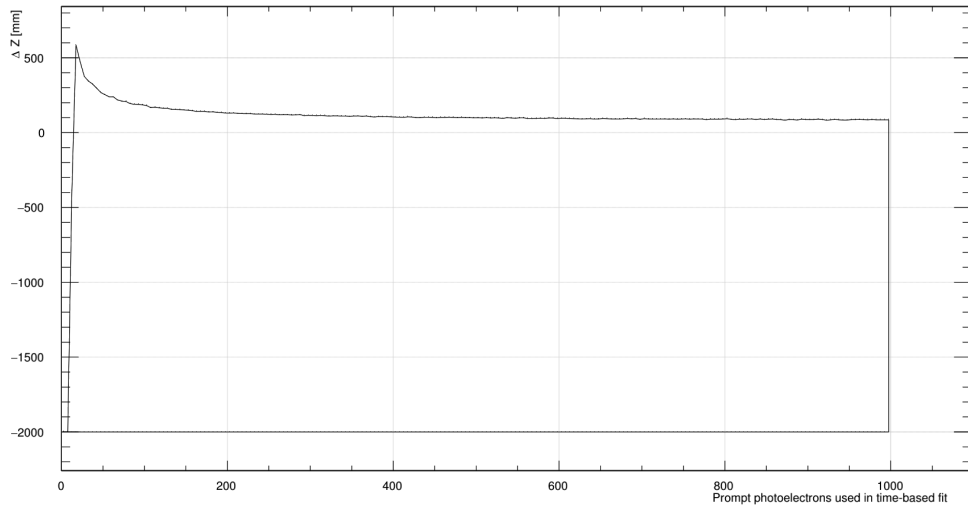


Figure 3.6: This plot shows the cut box used for removing neck events from a data set. The vertical axis shows the difference between the reconstructed  $z$ -coordinate from the time-based and charge-based fitters. The number of prompt photoelectrons that are used in the time-based fit is shown on the horizontal axis. Any events with parameters outside the box (typically above the line) are removed as possible neck alphas.

### 3.3 Position Resolution

The reconstruction algorithms will have some inherent error that is caused by uncertainty in the fitted parameters, systematic effects in the detector, and the limited charge and/or timing information they receive. This can be characterized as the resolution of the fitter. Generally speaking, measuring this resolution requires knowing the true position of an event so that the reconstructed position can be compared against it. In other experiments, such as the Sudbury Neutrino Observatory (SNO), radioactive sources can be placed inside the detector volume at known locations. The particles produced by the source will interact with the target medium close to their point of emission, and this gives a reference with which they can compare the reconstruction.

However we are unable to do this in DEAP for two reasons. First, the only opening into the acrylic vessel is at the neck, and this is occupied with the cooling coils. Secondly, and more importantly, is the concern of contamination. Since we are operating a relatively small detector and are not circulating the Argon, introducing external materials constitutes a large hazard of adding radioactive contaminants that would reduce our sensitivity to a potential dark matter signal.

Resolution results can be found using Monte Carlo simulations, since the true position is known, but this is an imperfect method. The algorithms are trained using the Monte Carlo, so any differences between your data and your MC will not be accounted for, and thus performance of reconstruction in MC does not definitively reflect its performance in reality. It can only give you a rough idea of whether your reconstruction works in principle and what it can achieve in an ideal case. This underlies the fundamental reasons motivating the work done for this thesis project, which will be described in the following chapter.

## CHAPTER 4

### MEASURING POSITION RESOLUTION

Herein lies the primary component of this thesis: the development of a position resolution measurement methodology that uses real detector data. It came out of the work of former University of Alberta PhD candidate Thomas McElroy, who had been studying the effects of pile-up, caused when the detector is triggered from one event and a second event happens within the same time window. In order to create a data set from which he could analyze the properties of pile-up events and develop methods of removing them during data cleaning he created a program called COMBINEEVENT. This program would take two single events and add one into the other, preserving all of the timing and charge information. He also wrote a program that could do the opposite, taking a single event and splitting it up into two, which was predictably called SPLITEVENT (SE). At the charge of my supervisor, I worked to develop a reliable way of measuring the position resolution using this program.

#### 4.1 SplitEvent

The program takes one event and creates two randomized “pseudo-events” from the charges in the original event’s PMTs, resulting in two unique events that are known to have the same point of origin in the detector volume. By reconstructing the position of each pseudo-event and then comparing the results, and doing this over a large number of events distributed throughout the detector, a value for the resolution can be determined. As such this allows for a measurement of the resolution to be found using live data and not just Monte Carlo.

The program is very simple at the heart of it, with the splitting operation being carried out within a nested for loop. The data is structured in such a way that each event has a list of the PMTs that observed at least one charge pulse, each of which then has a list of the pulses with information on the timing and the number of photons.

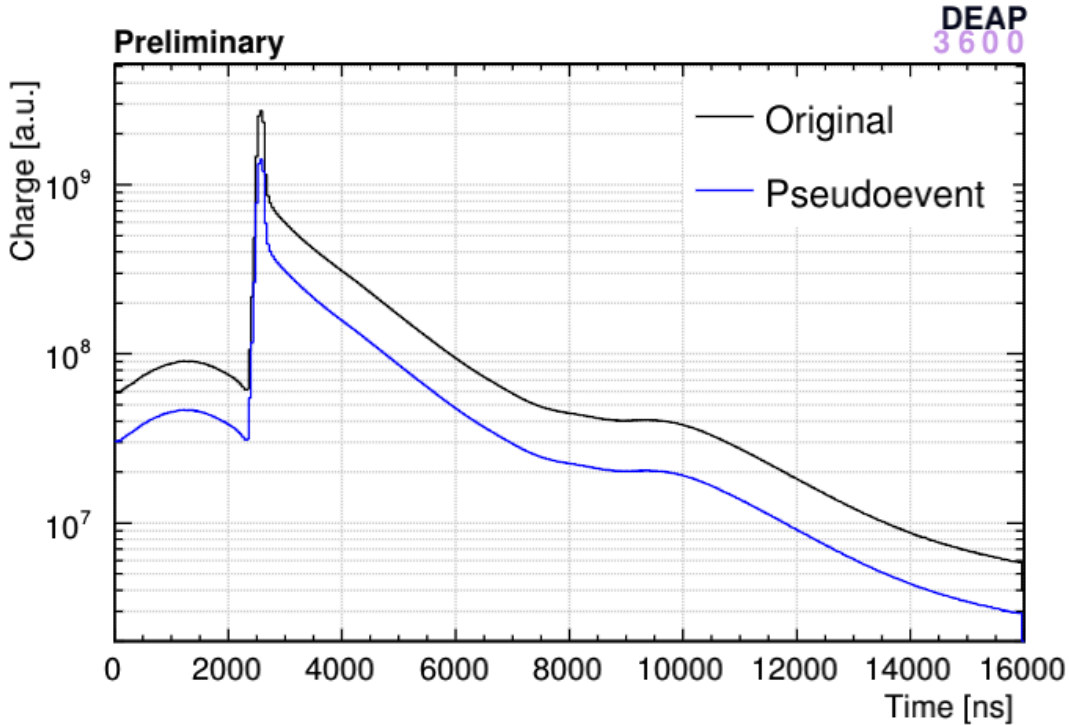


Figure 4.1: Summed histogram of events in a run showing PMT charge as a function of time. The pseudo-events have the same profile, only with half the charge.

The SplitEvent program first creates two clones of the original event data structure before looping through the pulses. Independent random numbers are thrown for each of the clones to decide how many PE are pruned from the pulse – or alternatively how many are kept, if you’re a pulse half full kind of optimist – such that on average each clone ends up with about half the total number of PE as the original. The result is two different pseudo-events that still exhibit many of the same characteristics as the parent event, for example the charge-time distribution shown in Figure 4.1. The creation of the pseudo-events is independent, but because they share the same parent there will still be some level of correlation between the two, approximately  $\frac{1}{4}$  when the chance is 50% as is considered here. Some preliminary tests looked at changing the pulse-keeping odds to reduce correlation, but this is left for future analyses to further study.

After being split, the two pseudo-events then have their position reconstructed, which can be done with any conceivable fitter, but will be done using the aforementioned charge and time based fitters in this document. There are a number of different ways the positions can be compared and initial efforts looked at just the spherical radius of each pseudo-event. Because the fiducial cut is performed on the radius, this was a logical first choice for testing the performance of the fitter. For each pair of pseudo-events  $z$  was calculated according to Equation 4.1, where  $r_i$  is the reconstructed spherical radius of the  $i^{th}$  pseudo-event, i.e. its distance from the center of the acrylic vessel. The value of this quantity, as well as its negative, was then binned into a one-dimensional histogram, an example of which can be seen in Figure 4.2. In doing this the distribution was forced to be symmetrical and centred at zero, allowing for better fits of the distribution.

$$z = r_1 - r_{\text{avg}} = \frac{r_1 - r_2}{2} \quad (4.1)$$

The function used for fitting the distributions, Equation 4.2, comes from Mark Boulay's PhD thesis on the SNO detector[42]. It consists of two parts, the first being a standard Gaussian distribution, and the second being a symmetrical exponential decay that helps in fitting the tails of the distribution. One of the parameters is the exponential decay fraction  $\alpha_e$ , which varies from 0 to 1, allowing for the distribution to be wholly Gaussian ( $\alpha_e = 0$ ) or entirely exponential decay ( $\alpha_e = 1$ ), although fitted values tend to be somewhere in-between.

$$R(d) = \frac{1 - \alpha_e}{\sqrt{2\pi}\sigma} \exp\left[-\frac{1}{2}\left(\frac{d - \mu}{\sigma}\right)^2\right] + \frac{\alpha_e}{2\tau} \exp\left[\frac{-|d - \mu|}{\tau}\right] \quad (4.2)$$

This equation shows the probability distribution of some generic quantity  $d$ , in this case referring to the difference in the chosen coordinate that is binned into the histogram. The mean of the distribution is represented by  $\mu$ , and the standard deviation and decay constants are given by  $\sigma$  and  $\tau$  respectively. To begin with, initial calculations found the half-width at half-max of the fitted distribution and additionally divided out the factor of  $\sqrt{2}$  owing to the distribution being comprised from two values,  $r_1$  and  $r_2$ . It should be stressed that this is not a proper measurement of resolution yet, rather

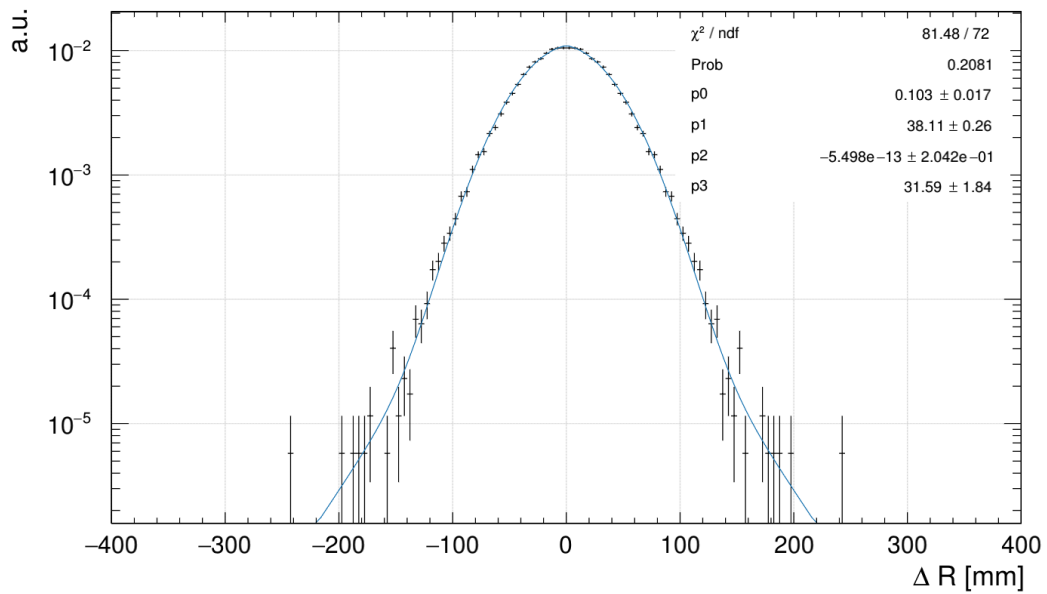


Figure 4.2: A histogram of the difference in spherical radius from pseudo-event average for events with average energy between 250 and 350 PE, and with original reconstructed radius between 300 and 350 mm.

it is the width of the  $z$  distribution, which we will refer to as the radial parameter  $\sigma_z$ .

It is not enough to calculate only a single value for the radial parameter, but rather one must find  $\sigma_z$  for specific areas of the detector volume and at specific energies, as both parameters are expected to affect the reconstruction. The average energy of the pseudo-events was used to place events in bins 100 PE wide, while the reconstructed radius of the original parent event was used for binning events in radius. The parent event's radius was used for this rather than the average pseudo-event radius because of systematic effects at the centre and the surface that artificially forced  $\sigma_z$  to be small, as seen in Figure 4.3. If binned by average pseudo-event radius, then as an example it would be necessary to have both pseudo-events reconstruct close in radius when near the center, otherwise the average would be larger and it would be placed in a higher bin. Similarly for the bin near the surface, ranging from 800 mm to 850 mm, it would not be possible to have anything greater than a 100 mm difference. Compare these two cases to bins somewhere in the middle values of radius (R), such as 400 mm to 450 mm and it becomes clear that a pseudo-event pair could be placed here but be up to 800 mm apart in radius. This artificially broadens the distributions in the middle R values. While the original event's reconstructed radius will still have some inaccuracy it is a better estimator than the average pseudo-event radius of the true position.

The results of such an analysis performed on data from a single run is shown in Figure 4.4. As was expected the radial parameter shows general improvement with increasing energy and with increasing radius. It should be noted that the empty bins in Figures 4.3 and 4.4 are the result of insufficient statistics for proper fitting of the distributions in those bins. Because the binning in R is done linearly, rather than in a cubic fashion, the volume of LAr each bin represents is not equal, with larger radius bins containing exponentially more LAr and therefore more Ar-39 events. This issue was alleviated by a later analysis where the one-dimensional distributions from multiple runs were summed together *before* calculating the resolutions. In this way sufficient statistics could be achieved at low radii to allow for a more accurate fitting of the distributions.

The next step was to see whether  $\sigma_z$  changed over time, which might signify a drift in the detector response that would not be accounted for with the static look-up tables

Run 20309

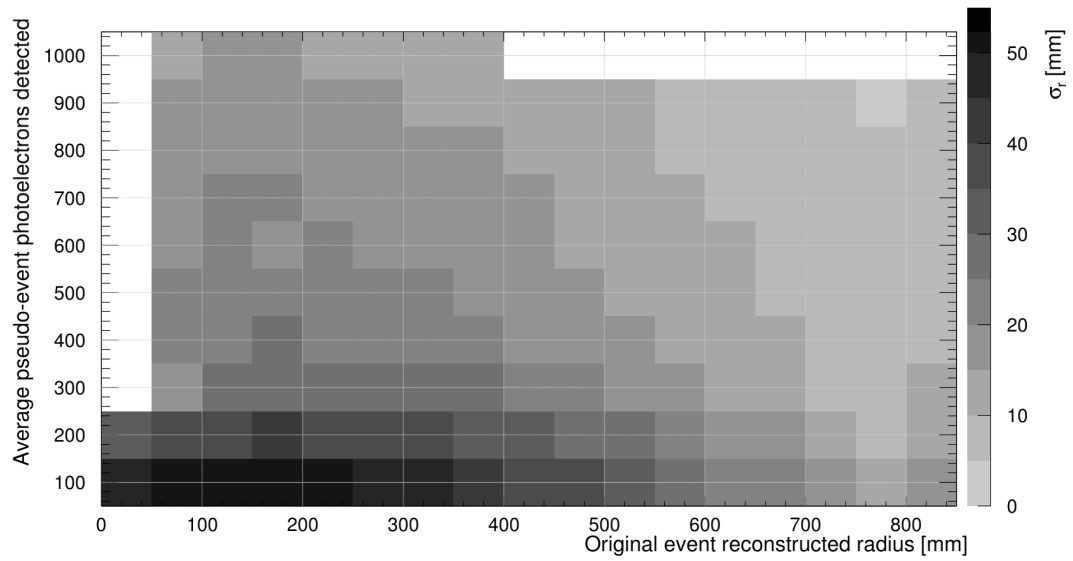


Figure 4.3: When binned by the average radius of the two pseudo-events it can be seen that the largest values of  $\sigma_r$  occur at radii of 200 to 300 mm.

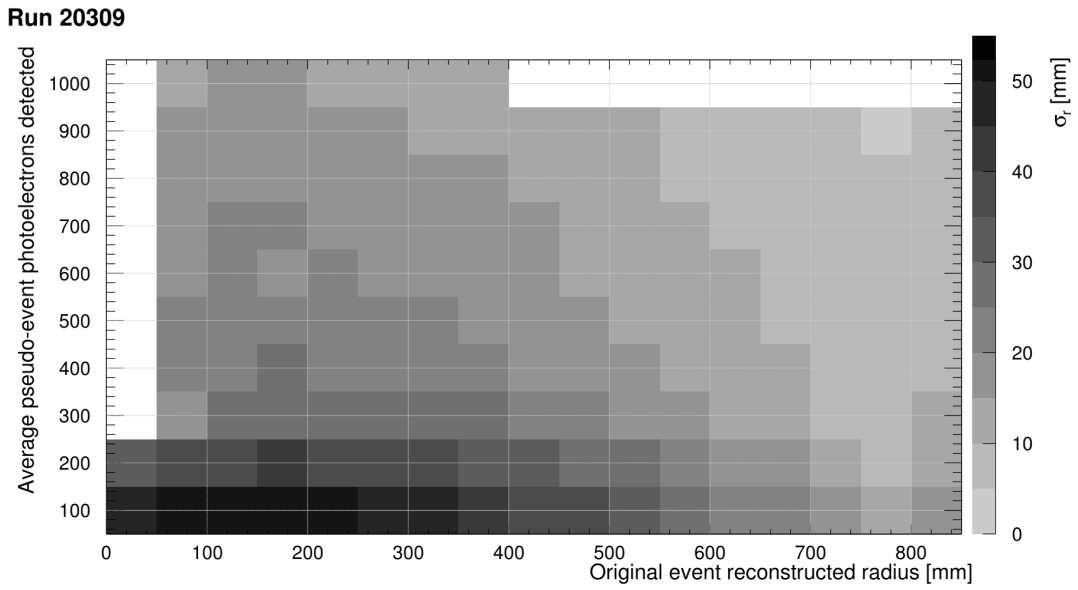


Figure 4.4: A plot of  $\sigma_z$  values using events from a single run, taken in August 2017. Empty bins are the result of insufficient bin entries for accurately fitting the distributions.

### Radial parameter for 550-650 qPE

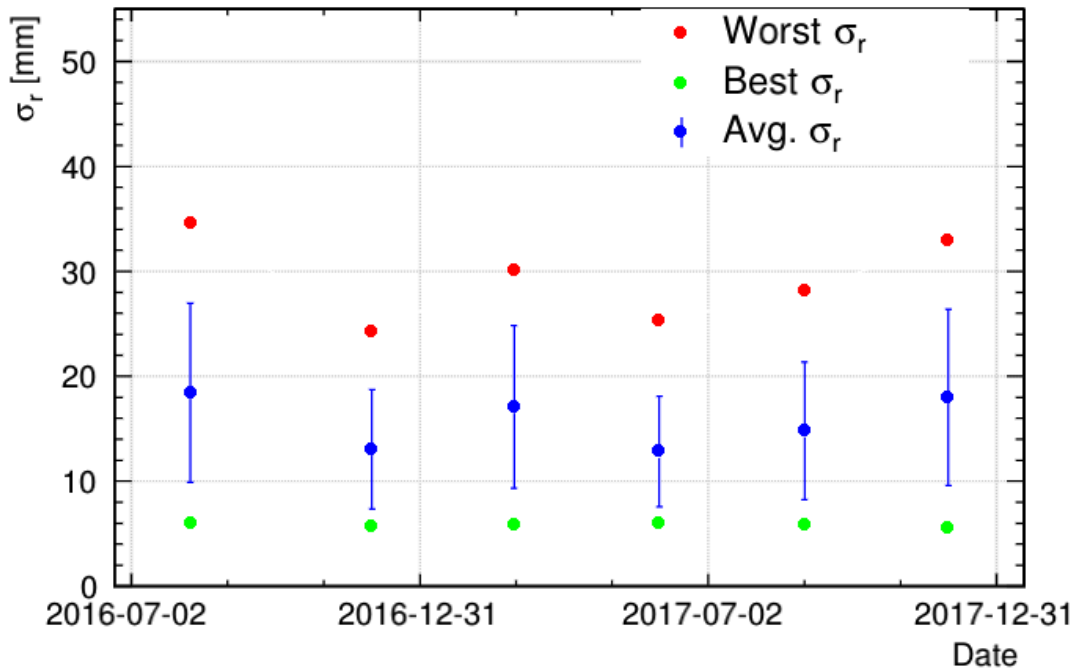


Figure 4.5: The best, worst and average  $\sigma_r$  values over all radii for a specific energy range, in this case 550 to 650 average pseudo-event photoelectrons, from six runs over a sixteen month time period. The error bars on the average points are the standard deviations.

of the charge-based fitter. Six runs over a 16 month period were selected and analyzed, with the best, worst and average values of  $\sigma_r$  for a specific energy range being plotted as a function of time. Figure 4.5 shows an example of this for events in the 550-650 PE range. While some variation is observed, it is still within the standard deviation, shown as the blue error bars on the average values of  $\sigma_r$ . It was therefore decided that this level of variation between runs was not a concern.

### 4.1.1 Radial Resolution

Following the initial tests measuring  $\sigma_z$ , I then switched to finding the proper resolution. This was done by finding the distributions of  $(x_1 - x_2)$ ,  $(y_1 - y_2)$  and  $(z_1 - z_2)$  and using their widths to calculate the resolution in spherical radius  $r$ . The derivation of the equation used to calculate this resolution is shown in Equations 4.3-4.7.

$$r = \sqrt{x^2 + y^2 + z^2} \quad (4.3)$$

$$\delta r = \frac{\sqrt{(x\delta x)^2 + (y\delta y)^2 + (z\delta z)^2}}{r} \quad (4.4)$$

$$\delta r = \sqrt{(\sin \theta \cos \phi \delta x)^2 + (\sin \theta \sin \phi \delta y)^2 + (\cos \theta \delta z)^2} \quad (4.5)$$

$$\overline{\delta r} = \frac{1}{4\pi} \int_0^{2\pi} \int_0^\pi \sqrt{(\sin \theta \cos \phi \delta x)^2 + (\sin \theta \sin \phi \delta y)^2 + (\cos \theta \delta z)^2} \sin \theta d\phi d\theta \quad (4.6)$$

$$\overline{\delta r} = \sqrt{\frac{(\delta x)^2 + (\delta y)^2 + (\delta z)^2}{3}} \quad (4.7)$$

The final equation, Eq. 4.7, shows that  $\delta r$  is the root-mean-square of the three coordinate uncertainties. Assuming that  $\delta x$ ,  $\delta y$  and  $\delta z$  are constant over  $\theta$  and  $\phi$ , i.e. assuming spherical symmetry of the detector, then the integral in Eq. 4.6 will yield the same result as Eq. 4.7. The equality between the two was confirmed numerically, and this therefore allows me to forgo doing the integral each time in favour of the simpler formula of Eq. 4.7.

As the fitted distribution is not simply Gaussian, the precise definition for the characteristic width ( $\sigma_{\text{eff}}$ ) is less clear. Since it is a combination of Gaussian and exponential decay I devised four possible equations to define the characteristic width as a combination of the widths of these two distribution types. These are shown in Equations 4.8–4.11, with two making the combination through a linear addition and the

other two adding in quadrature, with weighting determined by the exponential decay fraction parameter  $\alpha_e$ . Equations 4.8 and 4.10 use the fitted values of the parameters  $\sigma$  and  $\tau$ , while Equations 4.9 and 4.11 make use of the half-width-at-half-max (HWHM) using the substitutions from Equations 4.12 and 4.13.

$$\sigma_{\text{eff}} = (1 - \alpha_e)\sigma + \alpha_e\tau \quad (4.8)$$

$$\sigma_{\text{eff}} = \text{HWHM} \left( \frac{1 - \alpha_e}{\sqrt{\ln 4}} + \frac{\alpha_e}{\ln 2} \right) \quad (4.9)$$

$$\sigma_{\text{eff}} = \sqrt{[(1 - \alpha_e)\sigma]^2 + [\alpha_e\tau]^2} \quad (4.10)$$

$$\sigma_{\text{eff}} = \text{HWHM} \sqrt{\left( \frac{1 - \alpha_e}{\sqrt{\ln 4}} \right)^2 + \left( \frac{\alpha_e}{\ln 2} \right)^2} \quad (4.11)$$

$$\sigma = \frac{\text{HWHM}}{\sqrt{\ln 4}} \quad (4.12)$$

$$\tau = \frac{\text{HWHM}}{\ln 2} \quad (4.13)$$

To test the performance of each of these definitions, I first established a basic criterion of a good definition, which was that it consistently contained at least 68% of the area under the curve within  $\sigma_{\text{eff}}$ . This requirement comes out of a desire to adhere roughly to Gaussian statistics, even though it is not truly Gaussian. By using Monte Carlo techniques to generate random distributions of the form of Eq. 4.2 and performing an integration out to  $\sigma_{\text{eff}}$  according to each definition, the results can be seen in Figure 4.6. The two quadratic methods, shown in red and black, have broad distributions and on average contain less than 60% of the area. The green and blue populations come from the two linear methods and both average close to the desired 68%, however the HWHM method (Eq. 4.9) has a tail extending to lower percentages. The definition using parameters (Eq. 4.8) instead has a tail into the higher values and so was chosen

### Fraction of distribution contained within one $\sigma$

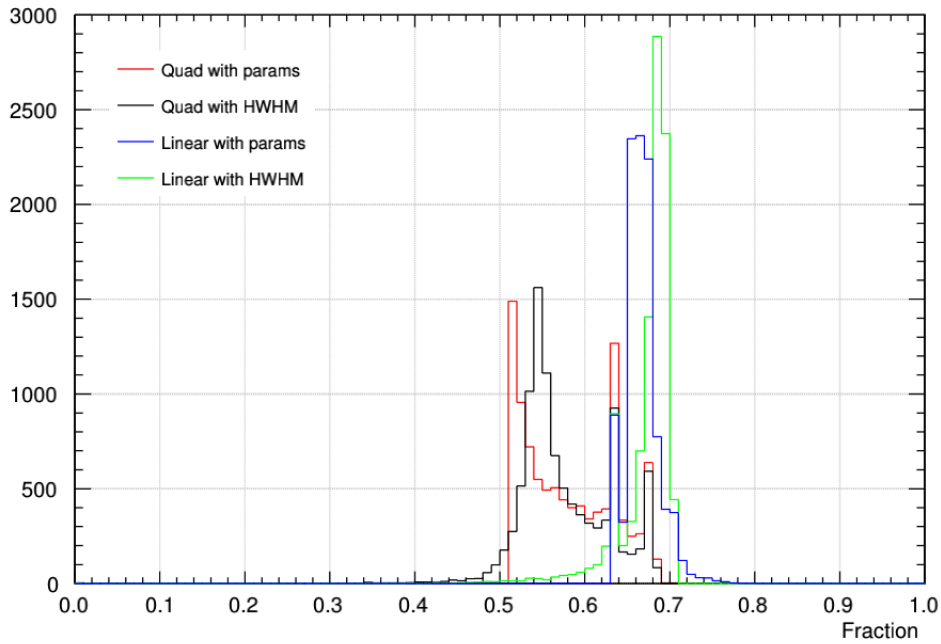


Figure 4.6: These four histograms show the range of integrated values within  $1 \sigma_{\text{eff}}$  of the randomly generated normalized distributions, for the four different definitions of  $\sigma_{\text{eff}}$ .

to be the best definition.

Figure 4.7 shows the resolution values found using live data from a total of 19 different runs. These results are included in the collaboration's 231-day exposure paper and are critical for demonstrating the effectiveness of the charge-based fitter and consequentially the efficiency of the fiducial cut used [31].

Following this analysis my attention was brought to the mathematical definition of the second central moment. This has the property of being the variance of any generic distribution function. The general definition of the  $n^{\text{th}}$  moment  $\mu_n$  is shown in Equation 4.14, where  $f(x)$  is the probability density function and  $\mu$  is the distribution's

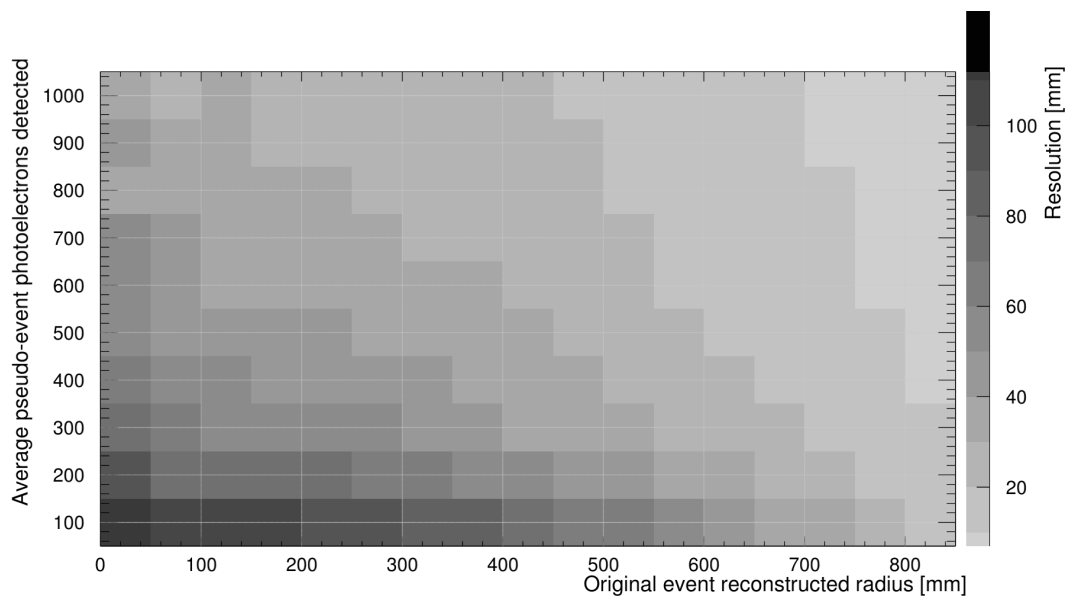


Figure 4.7: The data for this plot comes from 19 runs, all summed together before being fit with Eq. 4.2 and the resolutions calculated using Eq. 4.7 and Eq. 4.8.

**Fraction of distribution contained within one  $\sigma$**

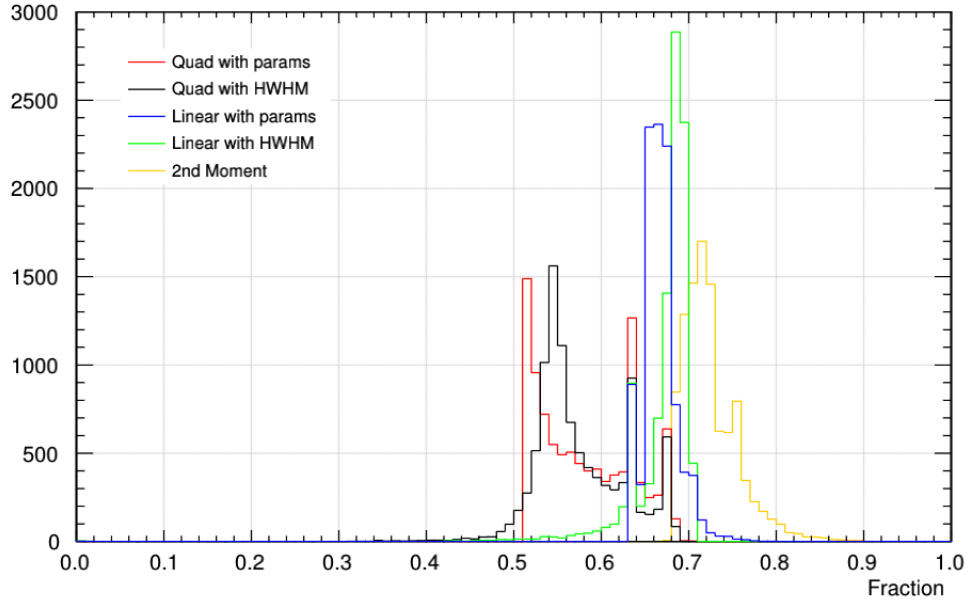


Figure 4.8: This shows the resulting integrated values when defining  $\sigma_{eff}$  according to the second central moment, compared with the previously mentioned methods.

mean.

$$\mu_n = \int_{-\infty}^{\infty} (x - \mu)^n f(x) dx \quad (4.14)$$

This method was similarly applied to the randomly generated distributions and the resulting  $\sigma_{eff}$  integration can be seen in Figure 4.8. In these MC tests it showed considerably larger values and it was hypothesized that it would then lead to larger reported values for the resolution of data, however when applied to data the resolutions in most of the parameter space did not change significantly, see Figures 4.9 and 4.10. At the lowest energy bin and the extreme radial bins the relative difference to the linear parameter method was as great as 30% (Figure 4.11).

Another suggestion offered to me was to perform a direct integration of the distributions out to 68% rather than fitting. This again yielded very similar results to those

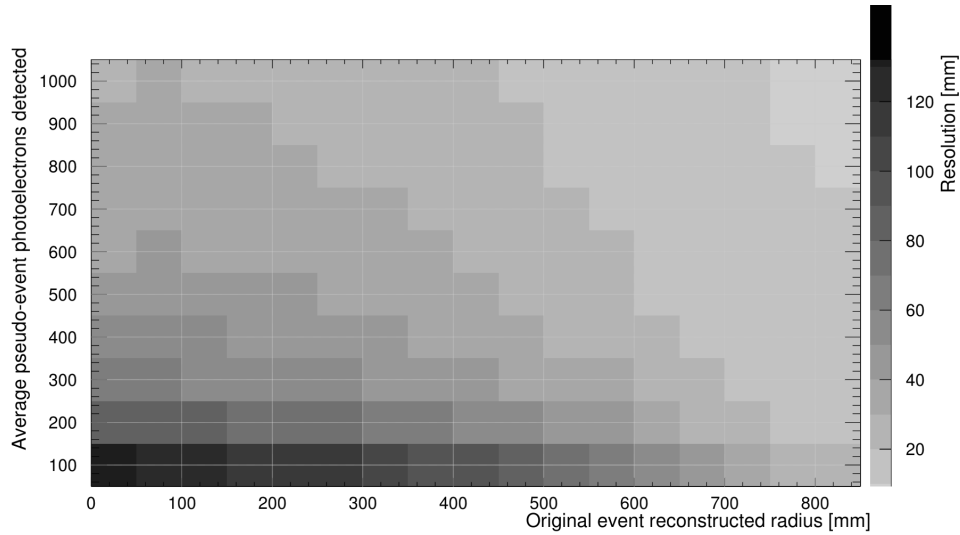


Figure 4.9: Here the resolution values have been calculated using the 2nd central moment method, as defined in Eq. 4.14 with  $n = 2$ .

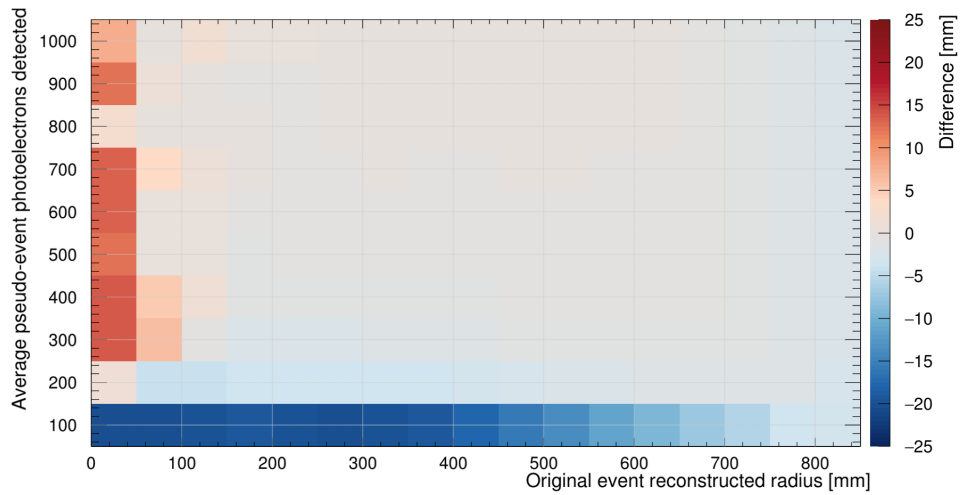


Figure 4.10: The horizontal and vertical axes are the same as in previous resolution figures, however now the colour axis is the difference between the resolutions found using the linear parameter method ( $\sigma_{\text{eff}}$ ) and using the 2nd central moment ( $\sigma_{2\text{cm}}$ ). Red bins are where  $\sigma_{\text{eff}}$  was larger, blue when  $\sigma_{2\text{cm}}$  was greater.

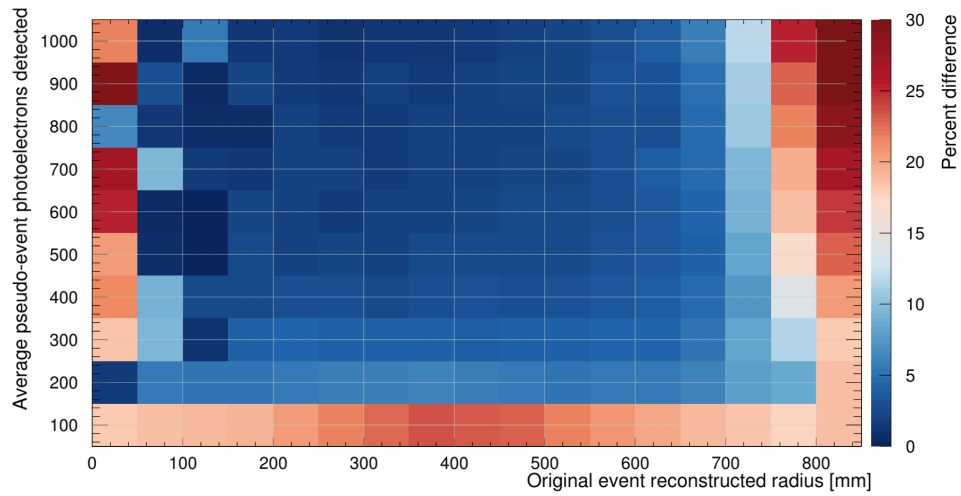


Figure 4.11: The colour axis shows the percent difference (PD) between the resolution values found using the 2nd central moment ( $\sigma_{2\text{cm}}$ ) and the linear parameter method ( $\sigma_{\text{eff}}$ ), defined as  $PD = \frac{|\sigma_{\text{eff}} - \sigma_{2\text{cm}}|}{\sigma_{\text{eff}}} \cdot 100\%$

found using Eq. 4.8, see Figures 4.12, 4.13 and 4.14.

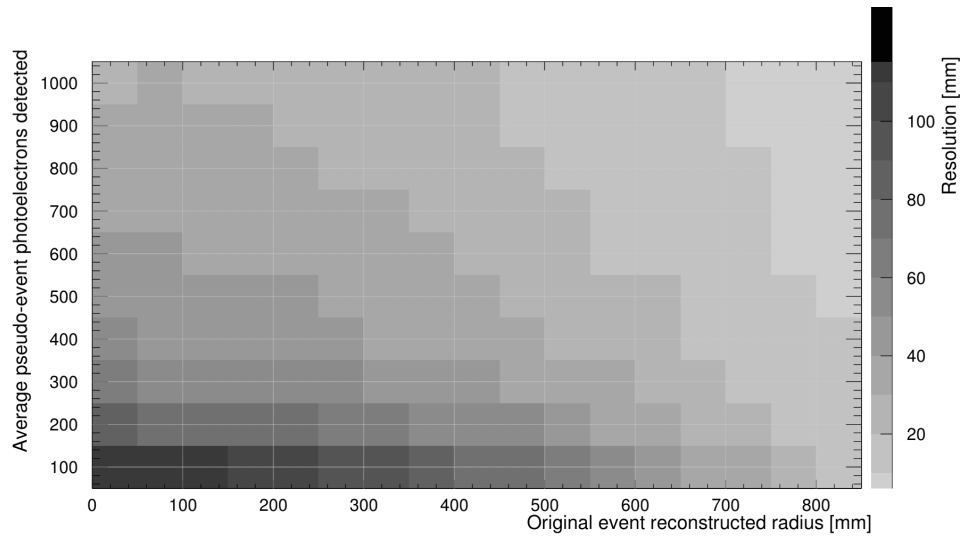


Figure 4.12: Here the resolution values have been found by integrating out from the mean until 68% of the distribution lies within  $1\sigma_{int}$ .

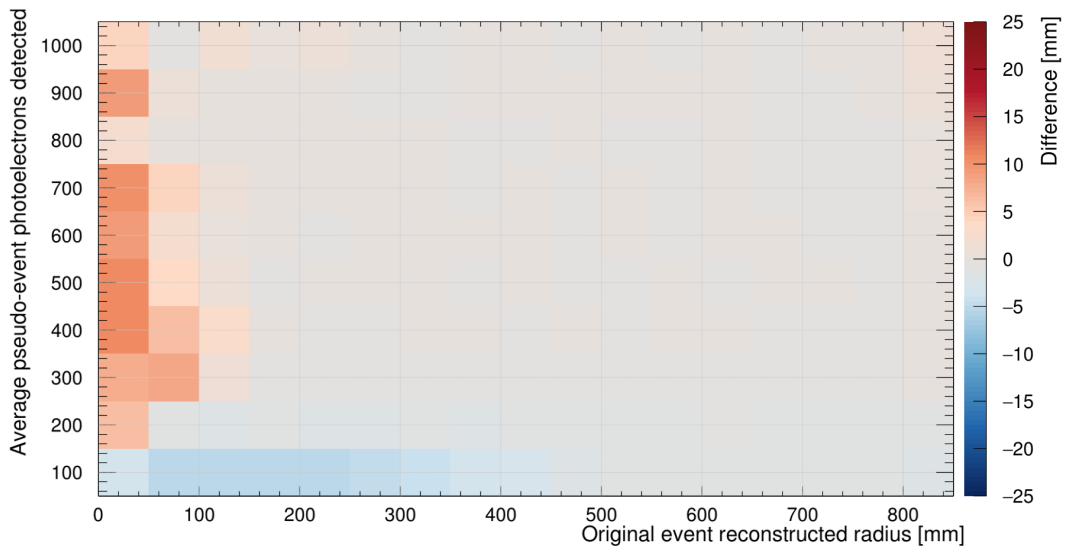


Figure 4.13: The horizontal and vertical axes are the same as in previous resolution figures, however now the colour axis is the difference between the resolutions found using the linear parameter method ( $\sigma_{\text{eff}}$ ) and the integration method ( $\sigma_{\text{int}}$ ). Red bins are where  $\sigma_{\text{eff}}$  was larger, blue when  $\sigma_{\text{int}}$  was greater.

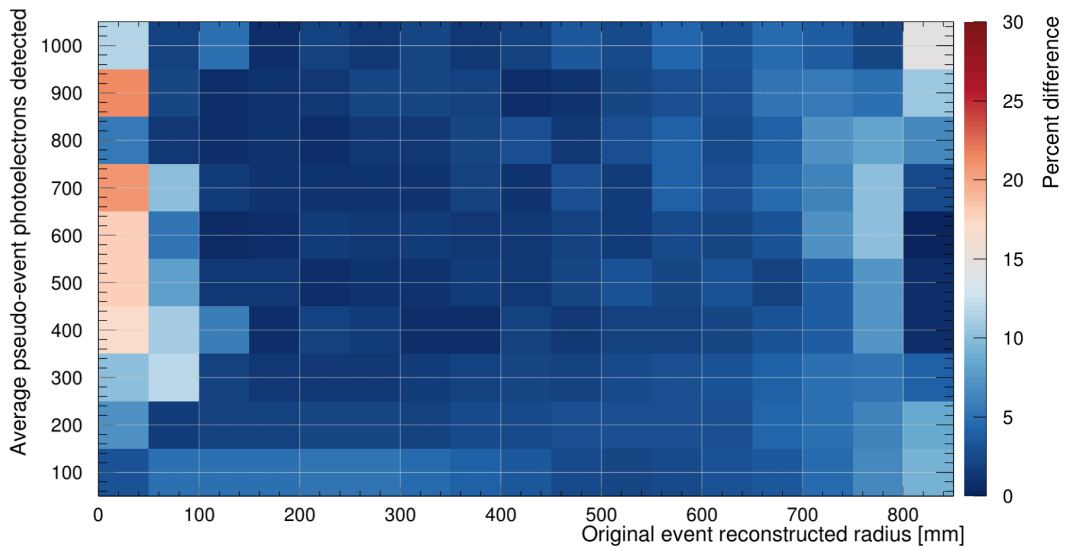


Figure 4.14: The colour axis shows the percent difference (PD) between the resolution values found using the integration method ( $\sigma_{\text{int}}$ ) and the linear parameter method ( $\sigma_{\text{eff}}$ ), defined as  $PD = \frac{|\sigma_{\text{eff}} - \sigma_{\text{int}}|}{\sigma_{\text{eff}}} \cdot 100\%$

#### 4.1.2 Evaluation

##### *Verification in Monte Carlo*

The same analysis was applied to Monte Carlo simulations of Ar-39 scintillation as an additional test of the resolutions measured with SPLITEVENT. This was then compared to the resolutions obtained from data. Close agreement was found between the two results as shown in Figure 4.15, generally within  $\sim 10$  mm.

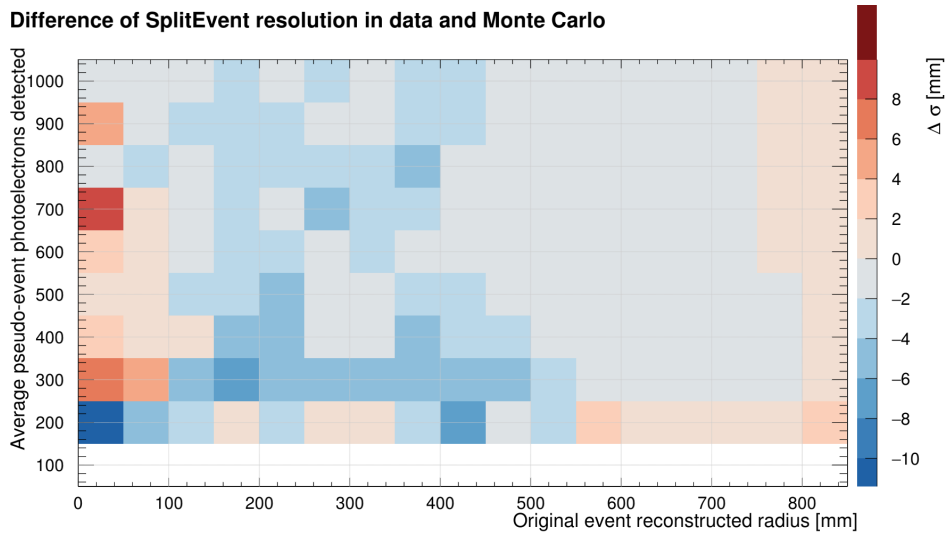


Figure 4.15: The colour axis of this plot shows the difference in obtained resolution measurements found using the SplitEvent method on data and in MC. Red bins represent where the resolution value was larger in data, blue where it was larger in MC.

A comparison was also made to the resolution values found using the MC truth position and the reconstructed position of the original event. This method was how resolution and fitter performance was tested in the past prior to SPLITEVENT’s development. The results can be seen in Figure 4.16 and the resolution values from SPLITEVENT are consistently smaller, by up to 44 mm in some bins. This is likely to be the result of bias in the reconstructed positions, which SPLITEVENT is blind to since both pseudo-events will experience the bias and on average cancel each other out. Figure 4.17 makes it clear there exists a subtle bias that pulls events outwards towards the surface of the detector. When events occur in the positive  $x$  hemisphere (the top half of the region in Fig. 4.17), the reconstructed  $x$ -coordinate trends towards larger, more positive values than the truth  $x$ . Similarly, in the negative  $x$  hemisphere, events tend to reconstruct at more negative values than truth. Since the resolution values are calculated using events binned by spherical radius, the distributions of  $X_{\text{MB}} - X_{\text{MC}}$  will be broadened due to this bias happening at both sides of the detector.

**Difference of resolution methods in Monte Carlo**

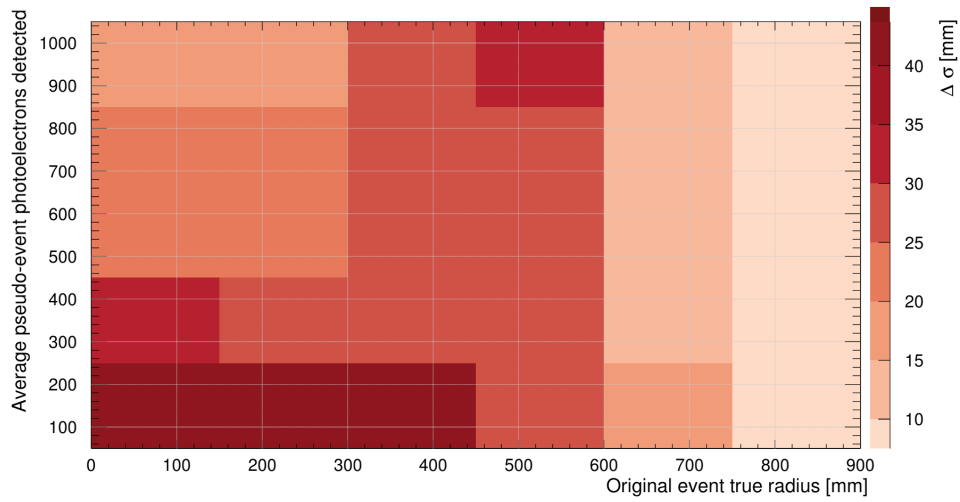


Figure 4.16: This plot shows the difference in the resolution in MC when calculated using SPLIT EVENT and when using the truth position. Red represents the SE resolution value being smaller. Note the coarser binning in radius and energy, which was necessitated by a limit of statistics in this analysis.

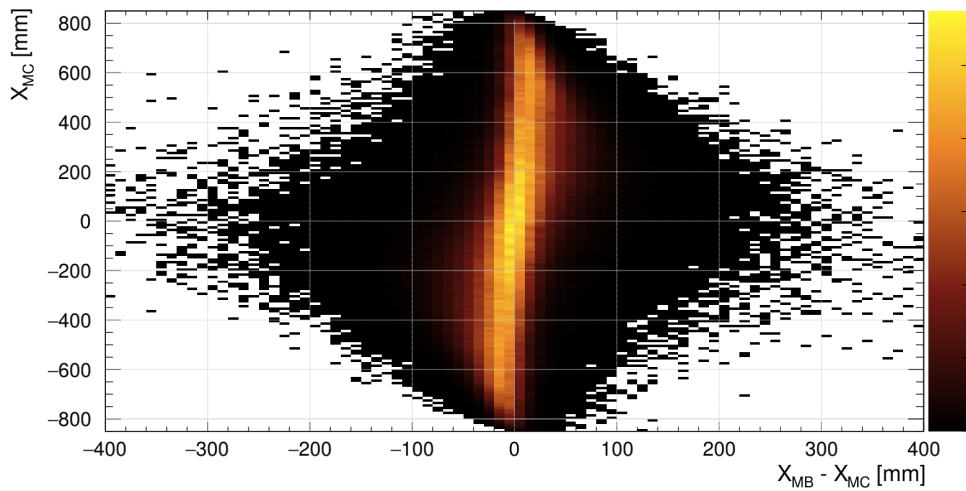


Figure 4.17: The bias of the charge-based likelihood fitter is evident in this plot. The vertical axis shows the true x-coordinate of the event, while the horizontal axis shows the reconstructed value of x minus the true x position.

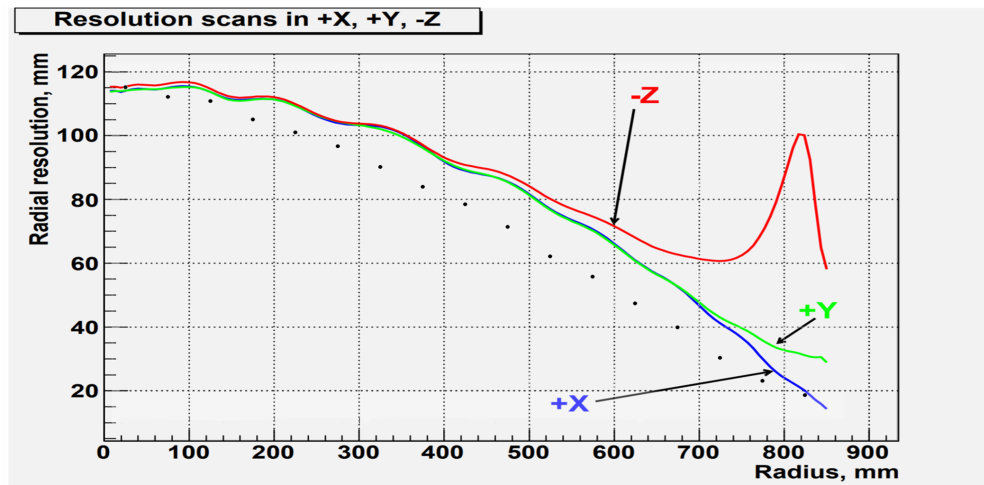


Figure 4.18: The three coloured lines are taken from the internal technical document describing the charge-based fitter, and show the predicted resolution values based on radius, but only in three Cartesian directions [40]. The data points are taken from Figure 4.12, and show the resolution values averaged over all directions at each radius.

### *Predictions*

In the original document detailing the design of the charge-based fitter, it is said that “resolution tends to be much better in the outer regions (i.e. closer to the photo-detectors)” [40] and that is clearly born out of the results of this project, see Figure 4.7. A figure from that document showed the expected radial resolution values as a function of radius along three separate axes (+x, +y and -z). That plot is shown in Figure 4.18 along with the actual data points from the low energy bin. The fitter performance exceeds the predicted values, and as these data are from the lowest PE bin they are also the largest in magnitude, resolution only improves with increasing energy.

Specifically, if resolution is purely statistical in nature then the expectation is that it should be proportional to the inverse square root of your statistics, i.e. the number of photoelectrons detected. While it evidently improves with increasing energy, it is not immediately obvious based on the 2-D resolution contours shown above, such as

Figure 4.7, whether that specific power law is followed. To test whether this was the case, the resolutions at a specific radius were plotted as a function of energy. In the first instance, Figure 4.19, the fit equation is of the form  $\sigma_{\text{eff}} = \frac{A}{\sqrt{E}}$ , where the power is fixed to the theoretical value of  $-\frac{1}{2}$ . In the second, Figure 4.20, the power is an additional parameter that is allowed to float ( $\sigma_{\text{eff}} = \frac{A}{E^B}$ ), and the experimental value comes out closer to  $-0.56 \pm 0.01$ . In both figures the original event's radius was between 500 mm and 550 mm. The deviation in the exponent may be from assigning all points a singular energy  $E$ , when in actuality each point represents events that had energies  $E_{\text{true}} \in (E - 50, E + 50)$ . Finer binning in  $E$  may then resolve the differences, but this is left as a task for future efforts. Nevertheless, some radii did have resolutions that more closely followed the expected power law, such as between 750 mm and 800 mm, which fit  $B = -0.49 \pm 0.03$ , and in fact “deviations from this law are always present to some degree, owing to PMT dark rate (at the lower energy end of the spectrum), PMT response saturation (at the higher end), or nonpointlike nature of the signal (especially for gammas)” [40].

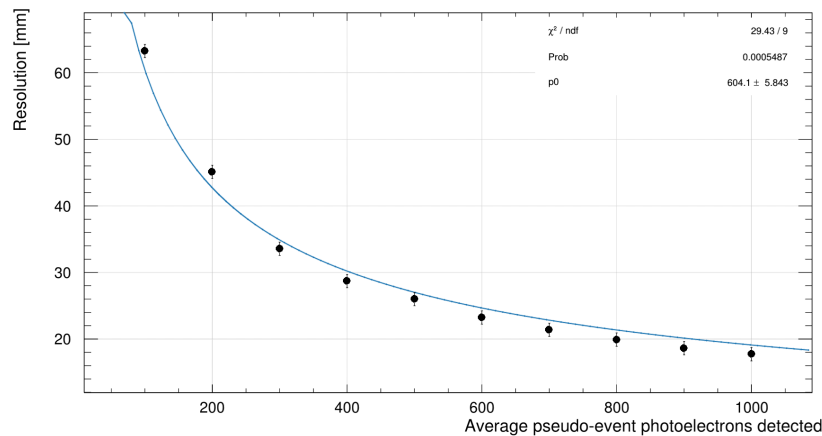


Figure 4.19: Considering cases where the original event reconstructed between 500 and 550 mm in radius, the calculated resolutions from the pseudo-events using the integration method are shown compared to their energies. The line fit to the data has one free scaling parameter.

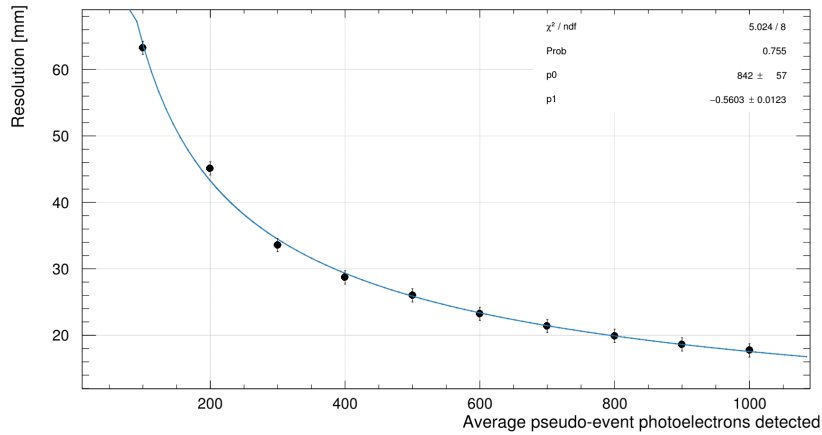


Figure 4.20: Considering cases where the original event reconstructed between 500 and 550 mm in radius, the calculated resolutions from the pseudo-events using the integration method are shown compared to their energies. The line fit to the data has two free variables, a scaling parameter and the exponent.

### 4.1.3 TIMEFIT2 Resolution

The same resolution analysis can be applied to the time-based position reconstruction algorithm on Argon-39 data. Figure 4.21 shows the results, and Figure 4.22 shows the difference with the charge-based values. As previously mentioned, the time-based method has greater values for the resolution than the charge-based fitter. As such its uses are primarily limited to the consistency cut to remove neck alphas, and also will soon be used for dust discrimination, which will be touched on in the next chapter.

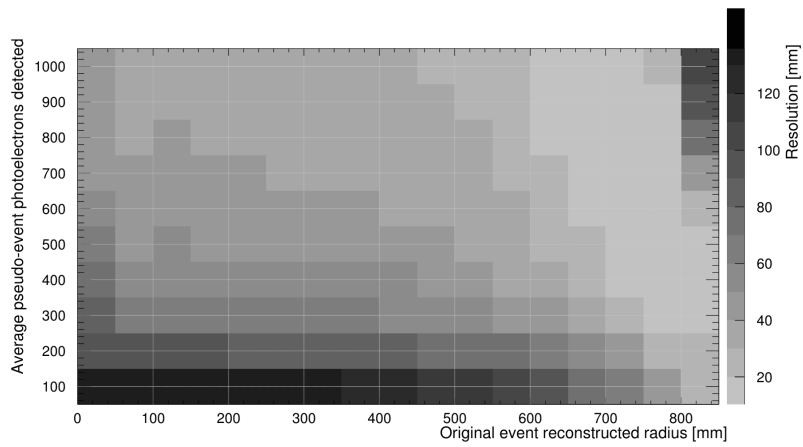


Figure 4.21: The SPLITEVENT resolutions measured for the time-based reconstruction algorithm TF2. Obvious systematic effects are visible at large radius and  $\sim 1000$  PE.

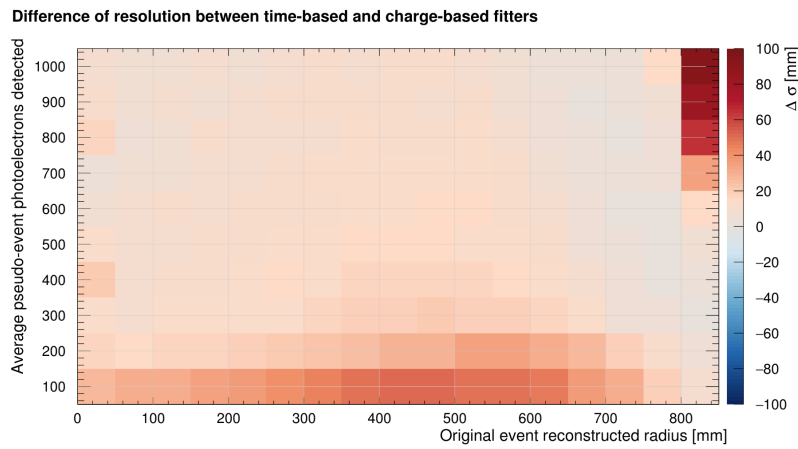


Figure 4.22: The TF2 resolution minus the MB resolution for each bin is shown on the colour z-axis. In every case, the time-based resolution was greater (worse) than the charge-based value.

## 4.2 MultiMB and Bias

In a similar vein to SPLITEVENT, I created a modified version of the previously described MBLIKELIHOOD charge-based fitter. This fitter used the same fitting methodology as MB but rather than performing the fit once it repeatedly fits pseudo-events generated within the processor itself. The goal was to study bias resulting from energy, so the pseudo-events were created to start with very little energy and with each loop contain a greater fraction of the original event's charge. The difference between reconstructed coordinates of the original and the pseudo-event can be placed into a histogram, and the mean of those distributions at different original reconstructed radii and pseudo-event energies can be binned into a 2-dimensional graph.

Figures 4.23, 4.24 and 4.25 show the results for parent events with energies between 950 and 1050 PE. As we saw in Figure 4.17, the bias in the fitter tends to be somewhat radial, so what is calculated for the bias figures here is the difference in the absolute values of the coordinates. This means that positive values are where the pseudo-event reconstructed closer to the center along the given coordinate. We do not see a substantial bias for most of the parameter space in any of the plots, except near the center of the detector where as the energy is decreased the events are pulled towards the surface. This is to be expected since as the number of photons is reduced the distribution of hit PMTs will appear less and less isotropic. Additionally this seems to hold for all three Cartesian directions, with the figures appearing quite similar in magnitude and the overall shape of the features.

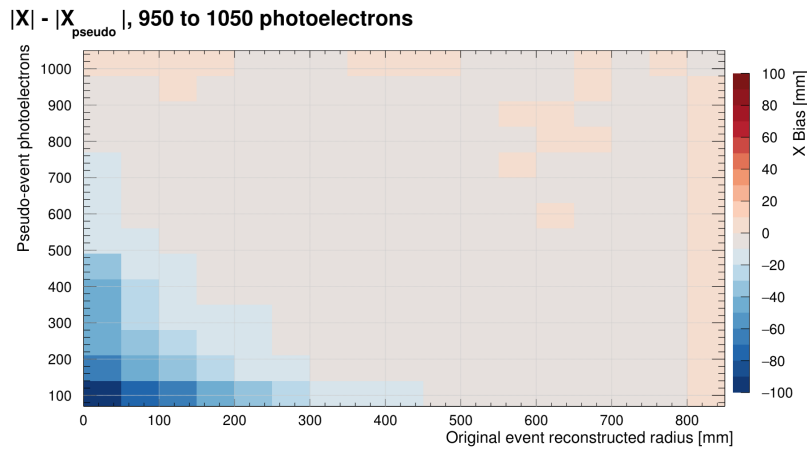


Figure 4.23: The y-axis shows the number of photoelectrons used to fit the pseudo-event's position. The z-axis colour scale represents the mean value of the distributions in the difference of the absolute values of the x-coordinates.

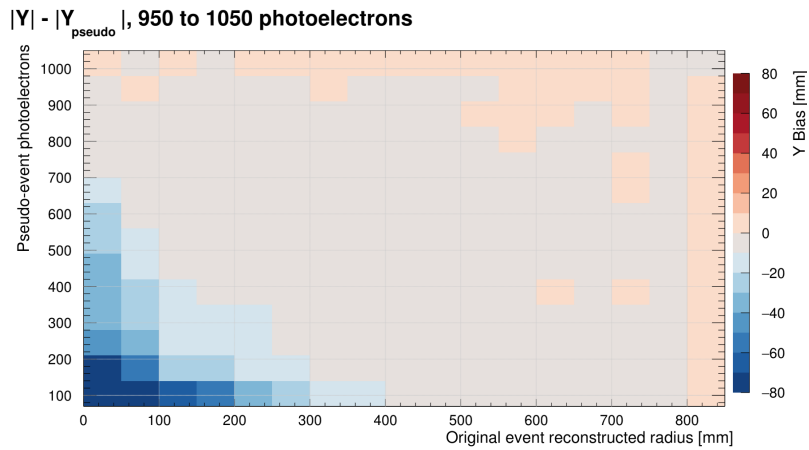


Figure 4.24: The y-axis shows the number of photoelectrons used to fit the pseudo-event's position. The z-axis colour scale represents the mean value of the distributions in the difference of the absolute values of the y-coordinates.

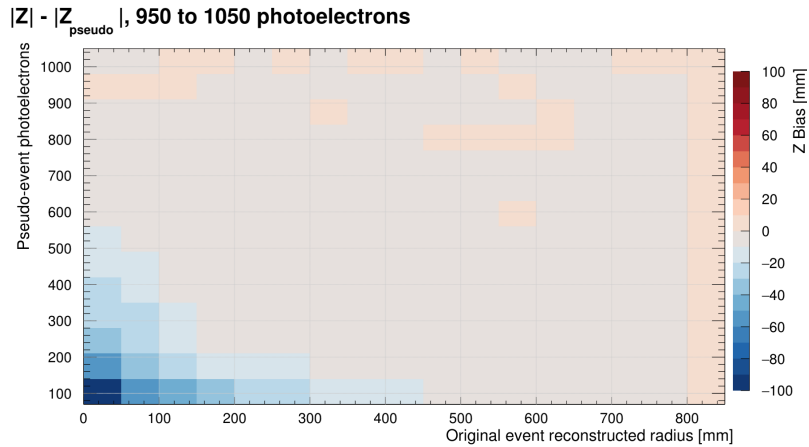


Figure 4.25: The y-axis shows the number of photoelectrons used to fit the pseudo-event’s position. The z-axis colour scale represents the mean value of the distributions in the difference of the absolute values of the z-coordinates.

#### 4.2.1 Continued Monitoring

The SplitEvent process described at the start of this chapter involves the complete processing of the pseudo-events that we apply to take our raw data and turn it into calibrated data for further analysis. This makes the output files containing the pseudo-events functionally equivalent to a standard “cal” file, allowing for any kind of study to use them. However this is also computationally expensive and takes up large amounts of storage, so for the purposes of position resolution measuring going forward I further modified MULTIMB to have a mode of operation that can effectively do the splitting itself. The standard charge-based processor has a mode where it loops through individual PMT pulses, very similar to what is done in the splitting program. So under this new mode MULTIMB will first perform the fit as per usual using all of the pulses, and will then repeat the fitting process twice more and have a 50% chance of using any specific pulse. The total value of PE used for each pseudo-event fit is stored, and so together this constitutes all the information used in the resolution studies described in this chapter:

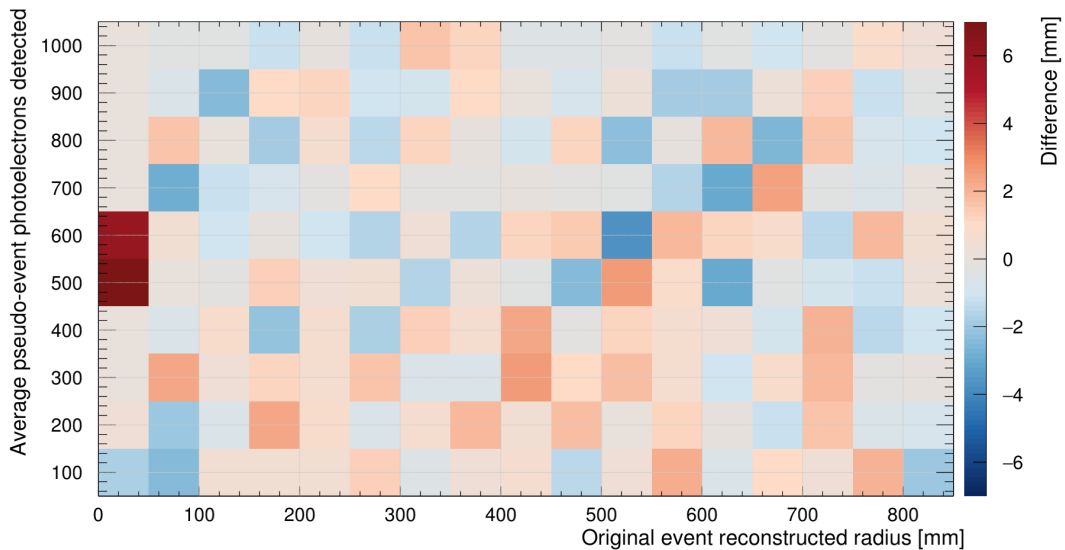


Figure 4.26: The difference in resolution values found by the standard SPLITEVENT process and those found using the MULTIMB process. Red is where SE values were larger.

- Original event reconstructed position
- Two pseudo-event reconstructed positions
- Average pseudo-event energy

Figure 4.26 shows the difference in resolution values found using the two methods: the complete SPLITEVENT pipeline and the simplified MULTIMB procedure. The differences are on the order of millimeters and appear random, suggesting they are the result of statistical errors and not anything systematic with the process. This is validation that the streamlined procedure with MULTIMB works and reproduces the same results.

This will greatly simplify the analysis pipeline for the resolution measurement, allow for continuous monitoring of the resolution values and testing of any new fitter improvements.

## CHAPTER 5

### DUST HYPOTHESIS

Dust in the detector is a possible source of alpha backgrounds that could leak into our ROI. Because the alpha only travels  $\sim 60\mu\text{m}$  in liquid Argon, and the dust could be on the order of  $100\mu\text{m}$ , the interactions happen close enough to the surface of the dust that the light is shielded. This has the effect of reducing the observed energy, obscuring our reconstruction of the event's total energy. Since alphas interact via nuclear recoil they also have a high  $F_{\text{prompt}}$  value similar to WIMPs, so if their measured energy is greatly reduced, they can appear inside our ROI.

A possible way to discriminate these events then is to look for this shadowing effect. While others worked to implement a dust model into the Monte Carlo, I started with some simple toy MC experiments to test possible discriminants and their effectiveness. This toy MC performed ray-tracing within a sphere, first from the event vertex to the AV surface, to then be re-emitted by the TPB and finally collected wherever they next intersected the AV. Regular events had an isotropic distribution of 200 photons, whereas dust events picked a random pointing vector and then only emitted light over the half-sphere facing that direction to simulate the shadowing effect.

Because the TPB re-emits light in a random direction this has the effect of minimizing the shadow when all of the detected light is considered, as after being converted to visible light the photon can travel back across the detector and hit a PMT within the shadowed region. As such the first step was to use photons that arrived roughly within the time-of-flight for UV from the PMT to the event vertex, which in this toy MC was just the truth position, but in data it would be the vertex fitted using the time-based algorithm. This restores the shadow and so the next step is to calculate something akin to the solid angle of the shadow from the event vertex. It is important to do this from the viewpoint of the event, because when close to the surface it is possible to still light up nearly all of the detector or only a single PMT, depending on where the alpha is emitted from the dust.

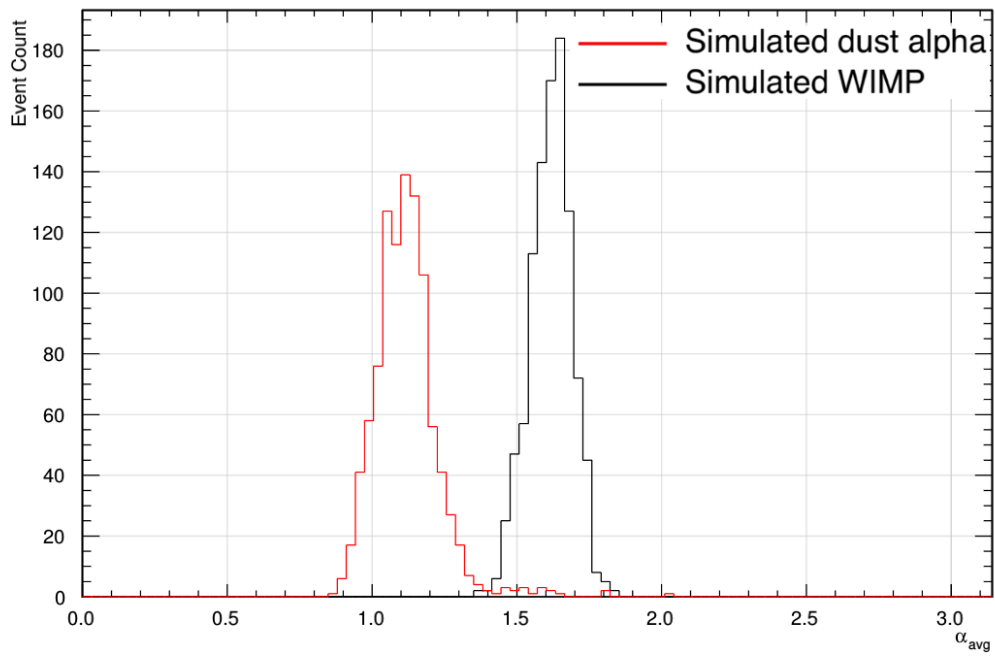


Figure 5.1: These two histograms show the distribution in the  $\alpha_{avg}$  parameter in the toy MC, with a clear distinction between the dust events (red) and the standard isotropic events (black) caused by the shadowing of the light by the dust particle.

I started by finding the average of the PMT vectors ( $\overline{r_{avg}}$ ), defined from the center of the AV and normalized to have a magnitude of 850 mm. Then the vectors pointing from the event vertex to this average location ( $\overline{d_{avg}}$ ) and to each PMT that fired ( $\overline{d_i}$ ) were found, and the angle between them ( $\alpha_i$ ) was calculated. Finally the average value of all the angles was found ( $\alpha_{avg}$ ), and the values were compared between dust and standard isotropic events. The results, seen in Figure 5.1, show a promising discrimination between the two classes. A cut applied at  $\alpha_{avg} = 1.4$  results in 99.5% acceptance of the signal and 98.7% rejection of the background. However, this was also an idealized case using truth values and neglecting various physical effects, and when applied to MC using full detector physics the discrimination was no longer as clear, refer to Figure 5.2.

Average alpha between average PMT position and all other PMTs, as seen from the fitted event vertex

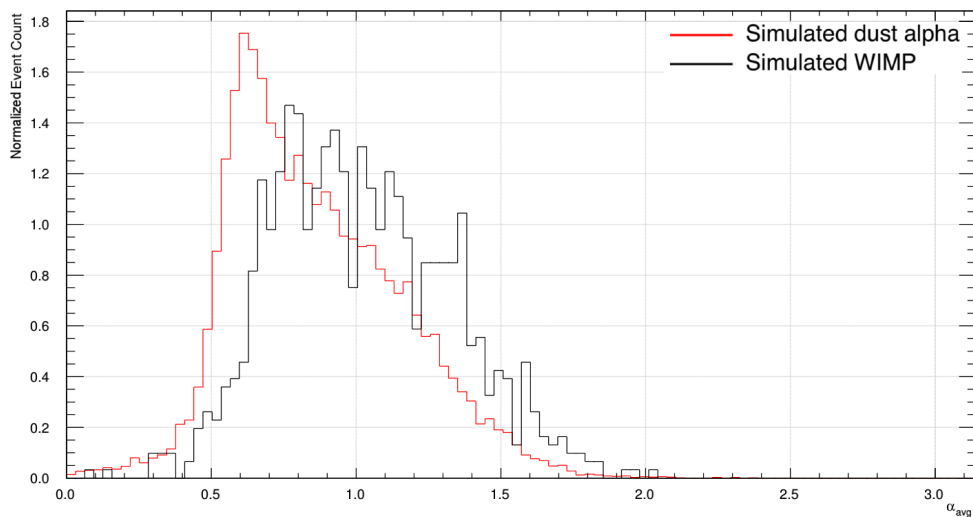


Figure 5.2: When using full detector physics, the same methodology as was used to find  $\alpha_{avg}$  before was applied to simulations of dust alphas and Argon 40 events. Significant overlap in the distributions is seen, greatly reducing the effectiveness of  $\alpha_{avg}$  as a discriminant.

Another University of Alberta researcher has been developing a similar method

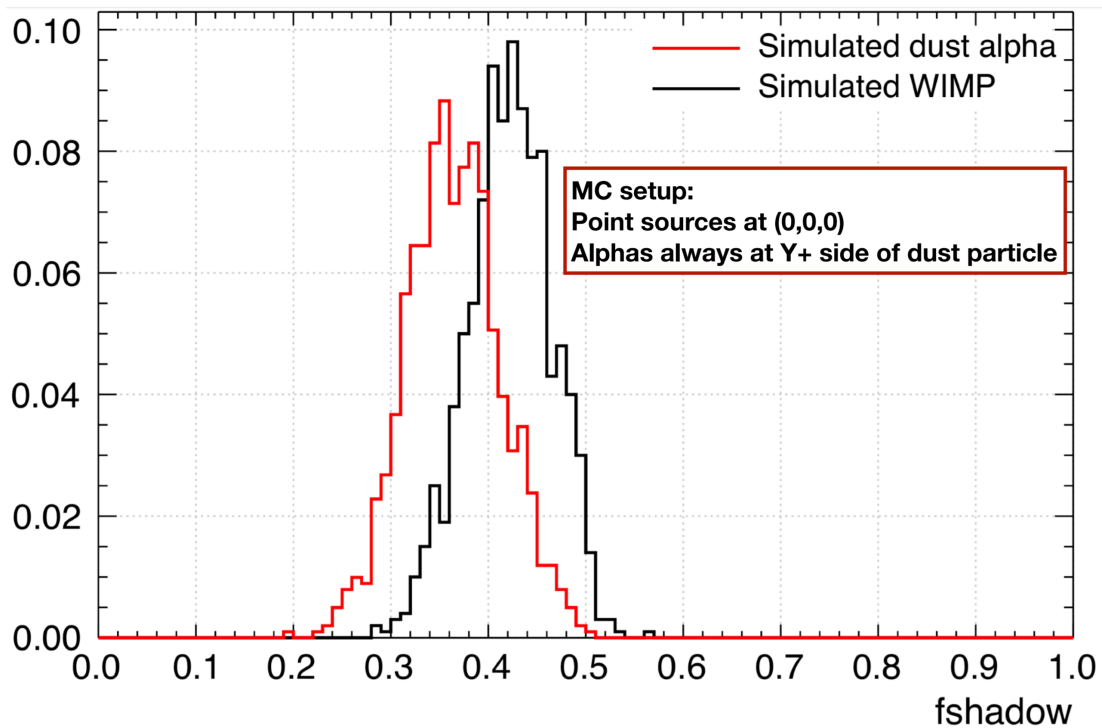


Figure 5.3: This shows preliminary work being done at the UofA for dust discrimination. Events were simulated at the center of the detector, and then the light angle was reconstructed and the backward charge fraction was calculated. This was done both for WIMP events (black) and for dust (red). Some distinction is visible. This work is still ongoing.

for dust discrimination. It reconstructs the most probable direction of light and then calculates the fraction of “backward” charge. This is the fraction of PE seen by PMTs that would be “behind” the event vertex when facing towards the reconstructed light vector. For events that produce isotropic distributions this value should be close to 0.5, but for dust we expect it to be reduced because of the shadowing. Figure 5.3 shows that some difference can be found between the two populations, but the overlap is still quite large. However these are early results and development continues on refining the reconstruction.

## CHAPTER 6

### CONCLUSION

The stated and primary goal of this research project was to develop a data-driven method of measuring the position resolution within the DEAP-3600 dark matter detector. Because of hardware restrictions as well as contamination concerns, radioactive sources inserted into the detector volume for the purpose of resolution measurements were not an option for DEAP. Instead a software method was necessary, and so by building off the work of other DEAP researchers I was able to create an analysis pipeline capable of achieving this goal via a process of event splitting. This method works by creating two pseudo-events, which are generated by randomly removing some of the light detected in a single event, resulting in two unique looking events which we can assume share a common origin in the detector. Through comparisons of the reconstructed positions of these pseudo-events we can therefore measure the resolution of the fitters, both charge and time-based. This process allows the use of the abundant Argon-39 signal in the detector, which is uniformly distributed throughout the volume of the liquid Argon.

The results achieved reflect what was predicted, showing an improvement in resolution closer to the AV surface and the resolution having an approximate inverse square-root relation to the event energy. The calculated resolution values demonstrate the precision of the fitters beyond initial projections and validates the fiducial cut used in the dark matter search, with resolutions at the fiducial boundary and ROI energies between 30 and 45 mm. Tests performed in Monte Carlo simulations further validates the measurement method, however it also shows that the reconstruction has some bias to which SPLITEVENT is blind.

Future work on this project will involve the continued monitoring of resolution values as well as the testing of fitter improvements. The effects of correlation between pseudo-events should also be further studied, as this may have slightly biased the resolution values. An analysis using high  $F_{\text{prompt}}$  events could also be of interest, however

obtaining a clear sample that is uniform in the detector is likely to be impossible.

## REFERENCES

- [1] M. K. G. Baghdady, “The discovery of neptune: A critical examination of the theory of leverrier,” PhD thesis, Aston University, 1980.
- [2] F. Zwicky, “English and spanish translation of zwicky’s (1933) the redshift of extragalactic nebulae,” trans. by H. Andernach, 2017. arXiv: 1711 . 01693 [astro-ph].
- [3] V. C. Rubin, “Dark matter in the universe,” *Proceedings of the American Philosophical Society*, vol. 132, pp. 258–267, 3 1988.
- [4] B. W. Carroll and D. A. Ostlie, *An introduction to modern astrophysics 2nd edition, The kinematics of the milky way*. Pearson, 2007, pp. 917,918.
- [5] G. M. Clemence, “Relativity effects in planetary motion,” *Proceedings of the American Philosophical Society*, vol. 93, no. 7, pp. 532–534, 1949.
- [6] A. Einstein and H. Minkowski, “Die grundlage der allgemeinen relativitatstheorie,” *Annalen der Physik*, vol. 354, pp. 769–822, 7 1916.
- [7] B. P. Abbott *et al.*, “Observation of gravitational waves from a binary black hole merger,” *Phys. Rev. Lett.*, vol. 116, p. 061 102, 6 2016.
- [8] M. Milgrom, “A Modification of the Newtonian dynamics as a possible alternative to the hidden mass hypothesis,” *Astrophys. J.*, vol. 270, pp. 365–370, 1983.
- [9] C. D. Paolo, P. Salucci, and J. P. Fontaine, “The radial acceleration relation (RAR): Crucial cases of dwarf disks and low-surface-brightness galaxies,” *The Astrophysical Journal*, vol. 873, no. 2, p. 106, 2019.
- [10] F. Schmidt, A. Vikhlinin, and W. Hu, “Cluster constraints on  $f(r)$  gravity,” *Phys. Rev. D*, vol. 80, p. 083 505, 8 2009.

- [11] D. Clowe *et al.*, “Weak lensing mass reconstruction of the interacting cluster 1e0657-558: Direct evidence for the existence of dark matter,” *Astrophysical Journal*, vol. 604, 2 2004.
- [12] M. Markevitch *et al.*, “Direct constraints on the dark matter self-interaction cross-section from the merging galaxy cluster 1e0657-56,” *Astrophysical Journal*, vol. 606, 2 2004.
- [13] M. White, “Anisotropies in the CMB,” 1999. arXiv: 9903232 [astro-ph].
- [14] N. Aghanim *et al.*, “Planck 2018 results. vi. cosmological parameters,” 2018. arXiv: 1807.06209 [astro-ph].
- [15] P. van Dokkum *et al.*, “A galaxy lacking dark matter,” *Nature*, pp. 629–632, 555 2018.
- [16] I. Trujillo *et al.*, “A distance of 13 Mpc resolves the claimed anomalies of the galaxy lacking dark matter,” *Monthly Notices of the Royal Astronomical Society*, vol. 486, no. 1, pp. 1192–1219, Mar. 2019. eprint: <http://oup.prod.sis.lan/mnras/article-pdf/486/1/1192/28390837/stz771.pdf>.
- [17] G. Bertone and D. Merritt, “Dark matter dynamics and indirect detection,” 2005. arXiv: 0504422 [astro-ph].
- [18] A. Arvanitaki, M. Baryakhtar, S. Dimopoulos, S. Dubovsky, and R. Lasenby, “Black hole mergers and the QCD axion at advanced LIGO,” *Phys. Rev. D*, vol. 95, p. 043 001, 4 2017.
- [19] J. L. Ouellet *et al.*, “Design and implementation of the ABRACADABRA-10 cm axion dark matter search,” *Phys. Rev.*, vol. D99, no. 5, p. 052 012, 2019. arXiv: 1901.10652 [physics.ins-det].
- [20] S. J. Asztalos, G. Carosi, C. Hagmann, D. Kinion, K. van Bibber, M. Hotz, L. J. Rosenberg, G. Rybka, J. Hoskins, J. Hwang, P. Sikivie, D. B. Tanner, R. Bradley, and J. Clarke, “Squid-based microwave cavity search for dark-matter axions,” *Phys. Rev. Lett.*, vol. 104, p. 041 301, 4 2010.

- [21] M. K. Gaillard, P. D. Grannis, and F. J. Sciulli, “The standard model of particle physics,” 1998. arXiv: 9812285 [hep-ph].
- [22] M. G. Aartsen *et al.*, “Search for neutrinos from dark matter self-annihilations in the center of the milky way with 3 years of icecube/deepcore,” *The European Physical Journal C*, vol. 77, no. 9, p. 627, 2017.
- [23] J. Kopp, “Collider limits on dark matter,” 2011. arXiv: 1105.3248 [hep-ph].
- [24] T. Kozynets, S. Fallows, and C. B. Krauss, “Modeling emission of acoustic energy during bubble expansion in pico bubble chambers,” 2019. arXiv: 1906.04712 [physics.ins-det].
- [25] D. Y. Stewart *et al.*, “Modelling electroluminescence in liquid argon,” *Journal of Instrumentation*, vol. 5, pp. 6–8, 2010.
- [26] S. Kang *et al.*, “DAMA/LIBRA-phase2 in WIMP effective models,” 2018. arXiv: 1804.07528 [hep-ph].
- [27] R. Bernabai *et al.*, “First model independent results from DAMA/LIBRA-phase2,” 2018. arXiv: 1805.10486 [hep-ex].
- [28] D. Ferenc *et al.*, “Helium migration through photomultiplier tubes – the probable cause of the DAMA seasonal variation effect,” 2019. arXiv: 1901.02139 [physics.int-det].
- [29] R. W. Schnee, “Introduction to dark matter experiments,” 2011. arXiv: 1101.5205 [astro-ph.CO].
- [30] S. Garbari, G. Lake, and J. I. Read, “Measuring the local dark matter density,” 2010. arXiv: 1001.1038 [astro-ph.GA].
- [31] R. Ajaj *et al.*, “Search for dark matter with a 231-day exposure of liquid argon using DEAP-3600 at SNOLAB,” *Phys. Rev. D*, vol. 100, p. 022004, 2 2019.
- [32] C. E. Yaguna, “New constraints on xenophobic dark matter from deap-3600,” 2019. arXiv: 1902.10256v2.

- [33] P.-A. Amaudruz *et al.*, “Measurement of the scintillation time spectra and pulse-shape discrimination of low-energy and nuclear recoils in liquid argon with deap-1,” *Astroparticle Physics*, vol. 85, pp. 1–23, 2016.
- [34] P. Lenard, “Ueber die lichtelektrische wirkung,” *Annalen der Physik*, vol. 313, pp. 149,198, 5 1902.
- [35] B. R. Wheaton, “Phillip lenard and the photoelectric effect,” *Historical Studies in the Physical Sciences*, vol. 9, pp. 299–322, 1978.
- [36] A. Einstein, “Concerning an heuristic point of view toward the emission and transformation of light (translation into english),” *American Journal of Physics*, vol. 33, 5 1965.
- [37] R. A. Millikan, “A direct photoelectric determination of planck’s ” $h$ ”,” *Phys. Rev.*, vol. 7, pp. 355–388, 3 1916.
- [38] A. J. Dekker, “Secondary electron emission,” in *Solid State Physics*, Pelgrave, London, 1981.
- [39] P.-A. Amaudruz *et al.*, “In-situ characterization of the hamamatsu r5912-hqe photomultiplier tubes used in the deap-3600 experiment,” *Nuclear Instruments and Methods in Physics Research Section A: Accelerators, Spectrometers, Detectors and Associated Equipment*, vol. 922, pp. 373–384, 2019.
- [40] B. Cai *et al.*, “DEAPStr2010x011: Surface background control in DEAP-3600,” *Internal Document*, 2010.
- [41] S. Viel, Y. Chen, *et al.*, “DEAPStr2018x006: Position reconstruction in DEAP-3600,” *Internal Document*, 2018.
- [42] M. Boulay, “Direct evidence for weak flavour mixing with the sudbury neutrino observatory,” PhD thesis, Queen’s University, 2001.

# Appendices

## APPENDIX A

### FANTASTIC CODES AND WHERE TO FIND THEM

The code for processing and analyzing data, as well as then calculating the resolution, can be found in this GitLab repository:

```
git@deap-gitlab.physics.carleton.ca:jwillis/willis_thesis.git
```

The included README file explains what each program does and how to use it:

`qsub_physics.pl` will submit rat jobs that use `SPLITINROOTPRODUCER` to create cal files for original events as well as each of the two pseudo-events

`fitmultimb_res_mode.mac` will run `MULTIMB` on a data file (needs pulse data in cal)

`SplitHist.cc` and `MultiRes.cc` are both for creating the 1-D histograms for  $x_1$ - $x_2$ ,  $y_1$ - $y_2$  and  $z_1$ - $z_2$ . The former handles files created by `SPLITINROOT`, the latter those processed with `MULTIMB`. Both are compiled by the included `Makefile`. The file `qsub_multires.pl` will allow for submission of `MULTIMB` jobs, but requires minimal changes to make it submit `SplitHist` ones instead. Use `hadd` to combine all of the individual files created for each (sub)run into a single file.

`CalculateResolutionXYZ.cc` will take that single file from either `SplitHist.cc` or `MultiRes.cc` and calculate the radial resolution using those  $x$ ,  $y$  and  $z$  distributions. Run with:

```
.x CalculateResolutionXYZ.cc (runnum, "MB" or "TF2", resMode)
resMode is either:
```

- 0 for the linear parameter based method described in my thesis
- 1 for the integration method
- 2 for the 2nd central moment method

If you've combined multiple runs together, I simply used a naming scheme of

“Combined\_SplitHist\_nSCBayes.root” and then runnum is set to 0 to access this file.

The “SplitHists” directory has all of my SplitHist data.

The “OldStuff” directory includes a hodgepodge of old code that is there if you want to look at my terrible coding habits and judge me.